

THE POPULATIONS OF CARINA. I. DECODING THE COLOR–MAGNITUDE DIAGRAM

JOHN E. NORRIS¹, DAVID YONG¹, KIM A. VENN², AARON DOTTER¹, LUCA CASAGRANDE¹, AND GERARD GILMORE³

ABSTRACT

We investigate the color-magnitude diagram (CMD) of the Carina dwarf spheroidal galaxy using data of Stetson et al. (2011) and synthetic CMDs based on isochrones of Dotter et al. (2008), in terms of the parameters $[\text{Fe}/\text{H}]$, age, and $[\alpha/\text{Fe}]$, for the cases when (i) $[\alpha/\text{Fe}]$ is held constant and (ii) $[\alpha/\text{Fe}]$ is varied. The data are well described by four basic epochs of star formation, having $[\text{Fe}/\text{H}] = -1.85, -1.5, -1.2$, and ~ -1.15 and ages $\sim 13, 7, \sim 3.5$, and ~ 1.5 Gyr, respectively (for $[\alpha/\text{Fe}] = 0.1$ (constant $[\alpha/\text{Fe}]$) and $[\alpha/\text{Fe}] = 0.2, 0.1, -0.2, -0.2$ (variable $[\alpha/\text{Fe}]$)), with small spreads in $[\text{Fe}/\text{H}]$ and age of order 0.1 dex and 1 – 3 Gyr. Within an elliptical radius $13.1'$, the mass fractions of the populations, at their times of formation, were (in decreasing age order) 0.34, 0.39, 0.23, and 0.04. This formalism reproduces five observed CMD features (two distinct subgiant branches of old and intermediate-age populations, two younger, main-sequence components, and the small color dispersion on the red giant branch (RGB)). The parameters of the youngest population are less certain than those of the others, and given it is less centrally concentrated it may not be directly related to them. High-resolution spectroscopically analyzed RGB samples appear statistically incomplete compared with those selected using radial velocity, which contain bluer stars comprising $\sim 5 - 10\%$ of the samples. We conjecture these objects may, at least in part, be members of the youngest population. We use the CMD simulations to obtain insight into the population structure of Carina's upper RGB.

¹Research School of Astronomy and Astrophysics, The Australian National University, Canberra, ACT 2611, Australia; jen@mso.anu.edu.au, yong@mso.anu.edu.au, aaron.dotter@gmail.com, luca@mso.anu.edu.au

²Department of Physics and Astronomy, University of Victoria, 3800 Finnerty Road, Victoria, BC V8P 1A1, Canada; kvenn@uvic.ca

³Institute of Astronomy, University of Cambridge, Madingley Road, Cambridge CB3 0HA, UK; gil@ast.cam.ac.uk

Subject headings: galaxies: abundances – galaxies: dwarf – galaxies: evolution
– galaxies: individual (Carina dSph)

1. INTRODUCTION

Since its discovery four decades ago by Cannon et al. (1977), the Carina dwarf spheroidal (dSph) galaxy has been the subject of enormous interest – driven by what it has to tell us about Carina’s formation and chemical enrichment, and the evolution of structure in the early Universe. Table 1 presents a list of some 20 major milestones that have contributed to our current understanding of the system from the above viewpoints¹. For recent comprehensive descriptions of the development of the extensive literature on Carina, we refer the reader to de Boer et al. (2014) and Kordopatis et al. (2016), and for an introduction to matters related to Carina’s population and abundance structures see Tolstoy et al. (2009) and Venn et al. (2012).

We begin here by briefly summarizing aspects of the available material that inform the impetus for the present work. In particular there is clear agreement that the majority of Carina’s stars are of intermediate age, with a smaller and well-defined older component. To cite de Boer et al. (2014) “Two main episodes of star formation occurred at old (>8 Gyr) and intermediate (2 – 8 Gyr) ages, both enriching stars starting from low metallicities ($[\text{Fe}/\text{H}] < -2$ dex)”. That said, and as the reader will see in Table 1, three and as many as six populations have also been suggested. Our starting point is that the extremely high quality photometric color magnitude diagram (CMD) of Bono et al. (2010) and Stetson et al. (2011) suggest to us that there were essentially four basic episodes of star formation, which we shall describe in Section 2. The excellence of the photometry and the observed tightness of Carina’s RGB lead to very strong constraints on age and chemical abundance distributions. Second, while the structure of the CMD is fundamentally driven by these two parameters, the CMD alone currently has the power to accurately constrain the age distribution function of the system. On the other hand, the chemical abundances ($[\text{Fe}/\text{H}]$ and $[\text{X}/\text{Fe}]$) needed to best determine the complete description of the system are provided by the brighter stars on the RGB. In this case, however, in contrast to the excellence of the photometric data, the available high-resolution spectroscopy is somewhat compromised by the faintness of Carina’s

¹Where possible, in the second column of Table 1 the first number refers to the discovery/seminal paper, while subsequent references refer to further important contributions.

RGB and currently of insufficient signal-to-noise (S/N) and too sparse and inhomogeneously analyzed to provide a definitive discussion of its chemical development and evolutionary history. To more fully address this issue we have sought to augment and homogeneously analyze high-resolution spectroscopic data to produce chemical abundances for a large sample of stars on Carina’s RGB. To this end we have assembled homogeneously determined relative abundances for 19 elements in 63 of its red giants.

We separate our investigation into two papers. The first, presented here, contains an analysis of the CMD. In the second (Norris et al. 2017, hereafter referred to as Paper II), we shall present the abundance results for the 63 red giants, which will be discussed in the light of age and abundance constraints from our analysis of the CMD in order to interpret the details of the above putative four populations that are present in the upper RGB sample.

1.1. Outline of the Present Work

In Section 2 we present the very high quality *BVI* photometry of Carina described by Stetson et al. (2011) and made available by P.B. Stetson (2014, private communication), and discuss the morphology of its (V , $B - I$) CMD in terms of the distinctive features that we shall use to constrain what we consider to be its four basic populations and their epochs of formation. We also compare this CMD with equally high quality data for the globular clusters M13, M92, and ω Cen. A comparison with the isochrones of Dotter et al. (2008) confirms the large differences between the intracluster age and abundance distributions of the globular clusters, on the one hand, and Carina, on the other. We discuss the implications of these differences for $[\text{Fe}/\text{H}]$ values determined for Carina from observations of the Ca II infrared triplet and calibrations based on Galactic globular clusters. Section 3 contains the core of our investigation, in which we present synthetic CMDs that reproduce the distinctive features of Carina’s CMD. These lead to estimates of the relative mass fractions of the four populations. Section 4 presents a discussion of the synthetic distribution functions of metallicity ($[\text{Fe}/\text{H}]$), $[\alpha/\text{Fe}]$, and age for stars on Carina’s upper RGB, which permit insight into the relative contributions of the four populations. We shall compare these results in Paper II with the observations of the sample of 63 Carina red giants based on our high-resolution spectroscopic abundance analyses. The results are summarized in Section 5.

2. PHOTOMETRY OF CARINA AND THE GALACTIC GLOBULAR CLUSTERS

2.1. The Carina CMD

Figure 1 presents the data of Stetson (2014, private communication) in the $(M_V, (B - I)_0)$ – plane for all of the ~ 31000 stars within an elliptical region centered on RA = 06 41 36 and Dec = –50 58 26 (2000) and elliptic radius $r_{\text{ellip}} = 13.1'$, with $e = 0.33$ and position angle 65° (Irwin & Hatzidimitriou 1995). To determine M_V and $(B - I)_0$ we adopted $E(B - V) = 0.06$ and $(m - M)_V = 20.05$, following Venn et al. (2012) and adopting $E(B - I) = 2.4 \times E(B - V)$. The left panel is the CMD, while in the right panel we show the Hess diagram, using contours. In what follows, we focus on the following five basic morphological aspects of this CMD: (i) the unexpected tightness of the RGB ($\sigma(B - I) \sim 0.07$ over the range $-2.5 < M_V < -1.0$) (see Section 2.1.1) given the large observed dispersion in iron abundance ($\sigma[\text{Fe}/\text{H}] \sim 0.4$ in our analysis for stars in this magnitude interval); (ii) the lower subgiant branch (SGB), at $M_V \sim 3.3$; (iii) the upper SGB, at $M_V \sim 2.7$; (iv) the main sequence stub above the upper SGB, at $(M_V, (B - I)_0) = (2.3, 0.5)$; and (v) the upper, bluer, and somewhat ephemeral (presumably) main sequence at $(M_V, (B - I)_0) = (2.0, 0.0) - (3.0, 0.2)^2$. We shall assume that each of features (ii) – (v) corresponds to a distinct stellar population and epoch of star formation in Carina, and that the parameters of these populations together produce a very tight RGB (feature (i)). In what follows we refer to stars in (ii) – (v) chronologically – as the “first”, “second”, “third”, and “fourth” populations, respectively.

²One might wonder whether Carina’s horizontal branch (HB) reaches blueward and fainter into the region of Carina’s upper main sequence and subgiant branch, and might contribute to what we have designated the “fourth population”. We are of the view that it is unlikely to play a major role, for two reasons. First, in Galactic globular clusters with the most blueward and fainter extended HBs, such as ω Cen and M13 (see the results of Bellini et al. (2009) and Stetson (<http://www.cadc-ccda.hia-ihp.nrc-cnrc.gc.ca/en/community/STETSON/standards/>) in our Figure 3) and NGC 6752 (see Campbell et al. 2013 based on data of Grundahl et al. 1999), the HBs reach down to $M_V \sim 2.0 - 2.5$, in contrast to Carina’s fourth population, which is clearly seen at $M_V = 3.0$. Second, inspection of our Figure 3 shows a very different M_V density distribution of the blue horizontal branch (BHB) stars of ω Cen and M13 as one moves from bright to fainter magnitudes than that seen for the collective BHB and fourth populations of Carina. An alternative suggestion is that the fourth population is made up of blue stragglers (Santana et al. 2016). We shall return to these points in Section 3.2.2.

2.1.1. The Tightness of Carina’s Upper RGB

In order to discuss the tightness of the upper RGB, we plot the Stetson et al. photometry of Carina’s upper CMD in Figure 2, highlighting the radial-velocity members from three independent investigations. In all three panels the small points represent all stars observed. These have been overplotted in the left panel with large red symbols for the 63 red giants having chemical abundances based on high-resolution model-atmosphere analysis (Paper II). In the middle panel the large green symbols stand for the radial-velocity members (at the 2.5σ level) from Koch et al. (2006); and on the right the large yellow symbols represent the radial-velocity members of Walker et al. (2009b). In the three samples, for stars brighter than $M_V = -1.0$, the RMS dispersions in $(B - I)_0$ about the quadratic least-squares fits (the black lines in the three panels) are 0.072 ± 0.007 mag for the Paper II sample (59 objects), 0.117 ± 0.009 mag for the Koch et al. (2006) sample (83 objects), and 0.100 ± 0.007 mag for the Walker et al. (2009b) sample (103 objects), respectively.

An intriguing conclusion from these data is that the RGB width of the Paper II sample is narrower than those of Koch et al. (2006) and Walker et al. (2009b) by some 4σ and 3σ , respectively. A likely cause of these differences is that while the results of Koch et al. and Walker et al. are based on statistically complete samples, that of Paper II comprises objects chosen to lie on the RGB in Carina’s CMD from a number of works, and is not complete. Roughly speaking, in the above magnitude range, the Paper II sample has a deficit of members blueward of Carina’s well-defined RGB at the $\sim 5 - 10\%$ level. The most obvious explanation of these bluer stars is that they are asymptotic giant branch (AGB) stars. In comparison, for globular cluster giant branch stars with $M_V \lesssim -1.0$, the AGB comprises some 20 – 30% of the upper giant branch (e.g., for M13 and M92 see our Figure 3; for M5, Sandquist & Bolte 2004; and for NGC 6752, Campbell et al. 2013). Furthermore, the existence of some nine carbon stars in Carina (Azzopardi et al. 1986) is consistent also with the presence of intermediate-age AGB stars. We shall return in Section 3.2.1 to the contaminating role of AGB stars in our comparison between the observed and synthetic CMDs of Carina, and in Section 3.2.3 we shall conjecture, based on our synthetic CMDs, that in some part they may be relatively-young (age ~ 2 Gyr) and on their first ascent of the RGB. Another explanation, suggested by Lemasle et al. (2012), in the context of spectroscopically selected samples observed at less than optimum S/N , is that there is an abundance bias in that stars of lower abundance are less likely to be analyzed than those having higher abundance.

Insight into the significance of the above color spreads is provided by the stellar isochrones of Dotter et al. (2008), which tell us that at $M_V = -1.8$ on the RGB of the isochrone $[\text{Fe}/\text{H}]/[\alpha/\text{Fe}]/\text{Age} = -1.5/+0.1/7.0$ (very roughly applicable to Carina; see de Boer et al.

2014 and our Figure 7) that the dispersion $\sigma(B-I)_0 = 0.072$ (where we have ignored the very small observational photometric errors at this magnitude) could be caused by a dispersion in $[\text{Fe}/\text{H}]$ of ~ 0.12 dex. This is well below the observed dispersion of $\sigma[\text{Fe}/\text{H}] = 0.33$ in the high-resolution spectroscopic abundances of the 63 star sample of Paper II. Confirmation of this effect is provided at fainter magnitudes on the RGB. In the red box in Figure 2, which lies below the above samples and spans the range $0.0 < M_V < 1.0$, the observed RMS dispersion in $(B-I)_0$ about the quadratic best fit to the RGB in $(B-I)_0$ is 0.038 mag (from 405 stars) (after a small quadratic correction of 0.014 mag to allow for random observational errors). For the above isochrone, this could be caused by a dispersion in $[\text{Fe}/\text{H}]$ of ~ 0.06 dex. As with the brighter sample considered above, this value is significantly smaller than that determined from the spectroscopic abundance analyses – the mean abundance for the Paper II 63 star sample is $\langle[\text{Fe}/\text{H}]\rangle = -1.59$, with dispersion 0.33, while for that of Koch et al. (2006) the corresponding values are -1.91 and 0.28 using the Zinn & West (1984) calibration, and -1.73 and 0.35 using that of Carretta & Gratton (1997). In summary, the upper RGB appears considerably tighter than one would expect from the observed $[\text{Fe}/\text{H}]$ values.

The obvious and simplest explanation of this conundrum lies in a degeneracy of compensating variations of the other two parameters that affect RGB morphology – age and $[\alpha/\text{Fe}]$ (e.g. Monelli et al. 2014; VandenBerg et al. 2015). A range in $[\alpha/\text{Fe}]$ values is a basic characteristic within individual dSph, and Venn et al. (2012) have demonstrated the existence of this effect in Carina. As Monelli et al. (2014) and VandenBerg et al. (2015) have shown, the tightness of the RGB could be explained by anti-correlations between $[\text{Fe}/\text{H}]$ and age and/or between $[\text{Fe}/\text{H}]$ and $[\alpha/\text{Fe}]$, such that the RGB sequences of the various populations have an anti-correlation between $[\text{Fe}/\text{H}]$, on the one hand, and age and/or $[\alpha/\text{Fe}]$, on the other, which conspire to produce RGBs that closely overlap. In Section 3.2 we shall examine the role of both age and $[\alpha/\text{Fe}]$, in addition to $[\text{Fe}/\text{H}]$, in seeking to decode Carina’s observed CMD.

2.2. A Comparison of Carina with Galactic Globular Clusters

All high-resolution chemical abundance analyses of Carina red giants to date report a large range in iron abundance, of order 1 dex between the extreme values (Shetrone et al. 2003; Koch et al. 2008; Venn et al. 2012; Lemasle et al. 2012; Fabrizio et al. 2012, 2015). In our homogeneous analysis of 63 red giant branch stars (Paper II) we find a range $-2.5 < [\text{Fe}/\text{H}] < -0.5$.

In Figure 3 we now compare Carina’s CMD with those of three Galactic globular clusters

– M13 and M92 (data from <http://www.cadc-ccda.hia-ihp.nrc-cnrc.gc.ca/en/community/STETSON/standards>) both of which show no spread in iron abundance ($\lesssim 0.03$ dex), with $[\text{Fe}/\text{H}] \sim -1.6$ and -2.3 (e.g. Kraft et al. 1997; Sneden et al. 2000), respectively, and ω Cen (data from Bellini et al. 2009), which presents a large abundance spread $-2.0 \lesssim [\text{Fe}/\text{H}] < -0.7$ – see Johnson & Pilachowski (2010). To focus the discussion, at the top of each of the four panels in the figure we have superimposed a box designed to encompass the observations of the Carina upper RGB, which will appear in several of the figures that follow.

We also superimpose Dotter et al. (2008) isochrones appropriate to M13 and M92 on the figure, having parameters $[\text{Fe}/\text{H}]/[\alpha/\text{Fe}]/\text{Age} = -1.6/0.4/13.8$ and $-2.2/0.4/13.8$ respectively, together with distance moduli and reddenings from Harris (1996)(2010 edition) (<http://physwww.physics.mcmaster.ca/~harris/mwgc.dat>), in panels (c) and (b). These parameters agree well with the literature values of $[\text{Fe}/\text{H}] = -1.53$ and -2.31 , respectively, of the Harris compilation; with $[\alpha/\text{Fe}] \sim 0.3 - 0.5$ (1D, LTE model-atmosphere modelling) as summarized by Sneden et al. (2000, Section 4.1) for globular clusters; $[\text{O}/\text{Fe}] = 0.5$ for halo stars (3D, NLTE modelling) down to $[\text{Fe}/\text{H}] \sim -2.5$ (Amarsi et al. 2015); and $[\text{Ca}/\text{Fe}] = 0.3$ (1D, LTE modelling) reported in Paper II for Galactic halo stars; and the ages of 13.0 and 13.25 Gyr reported by Dotter et al. (2010). The differences between the values we have adopted and those in the literature suggest that the Dotter et al. (2008) isochrones can be fit to globular clusters to within $\Delta[\text{Fe}/\text{H}] = 0.05 - 0.10$, $\Delta[\alpha/\text{Fe}] = 0.05 - 0.10$, and $\Delta\text{Age} = 0.7$ Gyr. One should also bear in mind the caveat of VandenBerg et al. (2015, Section 3.1) that the transformation from the physical parameters (e.g., effective temperatures) obtained from stellar evolution simulations to observed colors can lead to small fitting errors between observation and theory.

The M13 and M92 isochrones are also superimposed on the Carina data in panel (a). Finally, the isochrone for M13 is superimposed on the data for ω Cen in panel (d). The fit of the M13 isochrone to Carina on the upper giant branch is very poor, where there is little, if any, overlap between the RGB of M13 with that of Carina – in spite of the fact that the mean value for Carina of $[\text{Fe}/\text{H}] = -1.6$ is essentially the same as that of M13. This inconsistency graphically demonstrates the need for lower ages and/or lower $[\alpha/\text{Fe}]$ values in Carina, as discussed in the previous section.

Using the lower small boxes superimposed on the RGBs of M13, M92, and ω Cen in Figure 3, which cover the range $0.0 < M_V < 1.0$, we find color dispersions $\sigma(B - I) = 0.028$, 0.025 , and 0.077^3 , respectively, for these clusters, consistent with the small, if any,

³The widths of the boxes were chosen, by eye, to be sufficient to encompass the full color extent of the RGBs.

[Fe/H] and age spreads in M13 and M92, and the large abundance and variously reported age spreads in ω Cen (e.g., Joo & Lee 2013, Villanova et al. 2014).

2.3. Implications for [Fe/H] Abundances Determined with the Calcium II – Triplet Method

Analysis of the Ca II infrared triplet (at 8600 Å) has provided a powerful method for the determination of the [Fe/H] abundances of the Galaxy’s globular clusters and satellite dwarf spheroidal galaxies (dSph) (Armandroff & Da Costa 1991). There is, however, an important caveat concerning the resulting dSph abundances, in particular the results for Carina. When the method of [Fe/H] abundance determination for dSph systems is based on a calibration of the strength of the Ca II features as a function of the height a red giant lies above the horizontal branch in the CMDs of Galactic globular clusters (with their mono-modal morphologies) (for Carina see Koch et al. 2006), on the one hand, and the multiple-sequence CMD morphology and very different evolutionary history of the dSph, on the other, one should be concerned about the appropriateness of the calibration for Carina, which has the most complicated CMD morphology of the Galactic dSph for which data of sufficient quality are available⁴.

Specifically, the abundance of an individual red giant is given by an equation of the form $[\text{Fe}/\text{H}] = -2.706 + 0.326W'$, where $W' = W_{8542} + W_{8662} + 0.619(V - V_{\text{HB}})$ (Armandroff & Da Costa 1991), and W_{8542} and W_{8662} are Ca II equivalent widths and V and V_{HB} refer to the magnitude of the star and the horizontal branch having the same [Fe/H], respectively. For Carina, Koch et al. (2006) adopt $[\text{Fe}/\text{H}] = -2.77 + 0.38W'$, and an error in abundance of $\Delta[\text{Fe}/\text{H}] = 0.21\Delta(V - V_{\text{HB}})$, and report that an uncertainty in V_{HB} of +0.4 mag leads to an error of -0.07 dex. A further important uncertainty may also be inferred from our Figure 3. For example, at $[\text{Fe}/\text{H}] = -1.6$, the data for M13 demonstrate a different magnitude between globular clusters and Carina, such that at $(B - I)_0 = 2.3$, $\Delta M_V = M_{V\text{Carina}} - M_{V\text{GC}} = -0.4$ mag. In the Armandroff & Da Costa (1991) calibration, this corresponds to an abundance difference $\Delta[\text{Fe}/\text{H}] = \sim -0.1$ dex. As discussed above, this effect is driven by differences in the age and $[\alpha/\text{Fe}]$ distributions between Carina and the Galactic globular clusters. A further shortcoming of the use of Galactic globular clusters as calibrators is that the [Ca/Fe] distributions differ significantly between them and the dSph. For example, at $[\text{Fe}/\text{H}] = -1.5$, the difference between Carina and the halo is $\Delta[\text{Ca}/\text{Fe}] = [\text{Ca}/\text{Fe}]_{\text{dSph}} - [\text{Ca}/\text{Fe}]_{\text{Halo}} \sim -0.2$

⁴For comparison see de Boer et al. (2011, Sculptor), Okamoto et al. (2008a, Sextans), Okamoto et al. (2008b, Ursa Minoris), and Grillmair et al. (1998, Draco)

(see e.g., Tolstoy et al. 2009). One should not be surprised then to find errors in $[\text{Fe}/\text{H}]$ of ~ -0.3 dex in this formalism.

We investigate this further by comparing the (Ca II triplet based) $[\text{Fe}/\text{H}]$ abundances of Koch et al. (2006) with the high-resolution spectroscopic values of Paper II. In Figure 4, the leftmost panel, (a), presents the CMD for the 35 stars in common between the two investigations; the middle panel, (b), compares the $[\text{Fe}/\text{H}]$ values from the two investigations; and the rightmost panel, (c), plots the distance, $\Delta(B - I)_0 (= (B - I)_0 - (B - I)_{\text{RGB}})$, a star falls from the fiducial RGB in the CMD in panel (a) as a function of the abundance difference $[\text{Fe}/\text{H}]_{\text{Koch06}} - [\text{Fe}/\text{H}]_{\text{PaperII}}$. In panel (b) we also plot representative estimated abundance error bars, both of which are ~ 0.13 dex in size. In panels (b) and (c) the blue symbols represent outliers (defined in (c) where they comprise some 15% of the sample). Consideration of panel (b) shows that $\sim 10\%$ of the sample lie further than $\sim 3\sigma$ from the 1 – 1 line. We conclude that further consideration of this method is needed.

We would argue that a more appropriate approach to determining $[\text{Fe}/\text{H}]$ from measurements of the Ca II triplet would be a theoretical one using a model atmosphere analysis together with atmospheric parameters based on a star’s position in the CMD (see e.g., Norris et al. 2008; Starkenburg et al. 2010). That said, however, we note that even the results for Carina of Starkenburg et al. (2010, their Section 4.1) may be open to question, insofar as they report “We find that for a range of old ages, between 8 and 15 Gyr, the exact choice of the isochrone age does not significantly affect our results.” As we shall discuss in our Section 4, we find that some 75% of the Carina’s RGB stars have ages below 8 Gyr, suggesting that extrapolation in the determination of $[\text{Fe}/\text{H}]$ may have occurred for these objects. Given that a significant percentage of Carina stars appear to be younger than the ages used in the Starkenburg et al. (2010) analysis, we suggest that this calibration could be revisited.

In summary, Carina $[\text{Fe}/\text{H}]$ abundances determined from analysis of the Ca II infrared triplet use calibrations of questionable validity in the present context, and should be treated with caution.

3. SYNTHETIC COLOR MAGNITUDE DIAGRAMS

We seek to interpret the very high quality BVI photometry of Carina described by Stetson et al. (2011) and made available by P.B. Stetson (2014, private communication) by comparing its $(M_V, (B - I)_0)$ CMD against synthetic color-magnitude diagrams based on the isochrones of Dotter et al. (2008). In our analysis we adopt a set of Dotter et al. (2008)

isochrones defined by: $[\text{Fe}/\text{H}] = -2.45$ (0.05) -0.70 , $[\alpha/\text{Fe}] = -0.20$ (0.10) 0.40 , age = 0.8 (0.2) 15.0 (Gyr), and helium abundance $Y = 0.245 + 1.5*Z$ (where Z is the mass fraction of elements heavier than helium)⁵, together with a Salpeter mass function.

3.1. The Four Basic Populations

Figure 5 presents the $(M_V, (B - I)_0)$ CMD where the lower panel covers the magnitude range $-3.0 < M_V < 4.4$, and the upper panel covers the upper giant branch in the range $-3.0 < M_V < 0.0$. The leftmost panels contain the observational data, together with representative error bars (to the right) determined by averaging the (internal) photometric errors in V and $B - I$ available in the Stetson catalog. These errors are also presented in Table 2. As outlined in Section 2, we seek to model Carina in terms of four “basic” populations, to explain four of the observationally prominent features defined in Section 2.1. In the figure we use four boxes to define regions of the CMD that each contain stars from only one of these populations. These are the four boxes fainter than $M_V = 1.0$, and the faintest and reddest box contains the first population, with a monotonic progression to the brightest and bluest box which contains the fourth. The fifth and brightest box contains stars on the upper giant branch encompassing the 63 star RGB star sample for which chemical abundances are available based on high-resolution spectra to be presented in Paper II.

To determine the relevant stellar populations, we adopt the isochrones illustrated in the CMDs in the lower panels of Figure 5. Here, and in what follows, we consider two cases for $[\alpha/\text{Fe}]$: in the middle panels we present isochrones having constant $[\alpha/\text{Fe}] = 0.1$, while in the rightmost panels we permit $[\alpha/\text{Fe}]$ to vary over the range -0.20 to $+0.20$. In the lower middle and right panels the legends contain the basic $[\text{Fe}/\text{H}]/[\alpha/\text{Fe}]/\text{Age}$ parameters of the four populations. As will be described in more detail below, for each of the faintest three populations in the lower panels (the so-called first, second, and third populations), we adopt one basic isochrone chosen to pass in a representative manner through the stars in the population isolating boxes described above. We shall return to the fourth population below.

⁵We realize that substantial helium variations exist among the populations within several Galactic globular clusters such as, for example, ω Cen for which $\Delta Y \sim 0.12$ (Norris 2004; Piotto et al. 2005). To our knowledge there has been no suggestion that large helium variations exist in the dSph systems, and for economy of hypothesis we assume that none does.

3.1.1. *The First Three Populations*

We illustrate our procedure to determine ages and abundances for the case of constant $[\alpha/\text{Fe}] = 0.1$, describing the choice of the isochrone for each of the three populations in the defining boxes in the lower, middle panel. Given the tightness of the RGB, we firstly require that each isochrone passes as closely as possible through the point $(M_V, (B - I)_0) = (0.5, 1.62)$ on the RGB (as mandated by the observations); then for the first population, that it should also pass through $(M_V, (B - I)_0) = (3.25, 1.20)$; and for the second and third populations pass through $(M_V, (B - I)_0) = (2.72, 0.97)$ and $(2.50, 0.42)$, on their respective SGB and main-sequence stub, as seen in the observed CMD. The results of this process are presented in Figure 6. Here the relatively horizontal lines represent the (age, $[\text{Fe}/\text{H}]$) – loci of isochrones that pass through the boxes defining the SGBs and main-sequence stub of the first, second, and third populations, while the more vertical line crossing these three presents the locus for isochrones that pass through the RGB at $(M_V, (B - I)_0) = (0.5, 1.62)$.

The intersections in Figure 6 provide the ages and abundances of the isochrones of the first three populations in the middle panels of Figure 5, and presented in columns (2) – (4) of Table 3. For the variable $[\alpha/\text{Fe}]$ case, we chose $[\alpha/\text{Fe}]$ values of 0.2, 0.1, and 0.0 for the first through third populations, and for each of these the $[\text{Fe}/\text{H}]$ and age values were determined in a similar manner to that described above. The adopted values of $[\text{Fe}/\text{H}]/[\alpha/\text{Fe}]/\text{Age}$ for this case are presented in the rightmost lower panel of Figure 5 and in columns (6) – (8) of Table 3.

3.1.2. *The Fourth Population*

The simulation of the ephemeral, putative main-sequence, fourth population at $(M_V, (B - I)_0) = (2.0, 0.0) - (3.0, 0.2)$ is more challenging. Here there is an obviously larger observed spread in color at a given magnitude ($\Delta(B - I)_0 \sim 0.2 - 0.3$ at $M_V = 2.0$) than might be expected from errors in measurement of 0.025 dex (see, e.g., Table 2) and the dispersion of the Carina RGB of $\sigma(B - I)_0 \sim 0.04$, at the same magnitude. Further, the main-sequence feature exhibits a tantalizing suggestion of structure (in the range $2.0 < M_V < 3.0$). One might wonder if more than one sub-population exists within our so-called fourth population. As we shall see we are somewhat limited in our investigation by the fact that the minimum age in the set of isochrones we have chosen to use is 0.8 Gyr. With this background, we have adopted a single “basic” isochrone for the fourth population in the middle panels of Figure 5 having parameters $[\text{Fe}/\text{H}]/[\alpha/\text{Fe}]/\text{Age} = -1.2/0.1/1.4$ for the constant $[\alpha/\text{Fe}]$ case,

while in the rightmost panels we assume $-1.1/-0.2/1.4$ for the variable $[\alpha/\text{Fe}]$ case⁶. We shall address the nature of the fourth population further in Section 3.2.2.

3.2. Synthetic CMDs of the Basic Populations

3.2.1. First Approximation

First-order synthetic CMDs are presented in Figure 7, where the general layout is the same as in Figure 5. As before, the observational data for the total Carina sample are presented in the bottom left panel. To its right are synthetic CMDs based on the four “basic” populations shown in Figure 5 for fixed $[\alpha/\text{Fe}]$ (middle panel) and variable $[\alpha/\text{Fe}]$ (right panel). In Figures 5 and 7, and throughout this paper, red, green, blue, and magenta are used to refer to the first through fourth populations, respectively.

To produce the synthetic CMD, we drew magnitudes and colors at random from the Dotter et al. (2008) isochrones adopting the Salpeter mass-function. To these we added random observational uncertainties, for which we have presented representative values in Table 2. The lower panels of Figure 7 contain the five boxes described in Figure 5, which were chosen to isolate important representative populations in the CMD (the faintest four of which isolate samples unique to the four basic Carina populations). Also presented in the legend of the lower leftmost panel are the numbers of stars observed in the five sub-samples, corrected for background interlopers by using a nearby field some $25'$ from the center of Carina⁷. The corrections to the number of stars in the boxes isolating the first through fourth populations were 204, 115, 5, and 15, respectively, and 72 for the box on the upper RGB.

In preparing the synthetic CMD we chose stars at random for each of the four basic populations in turn, until we obtained the observed number of stars in the relevant box in Figure 5. Finally, we simulated field non-members by superimposing on the diagram the data from the nearby observed field mentioned above, which we added to the synthetic catalog. The synthetic CMDs are presented in the middle (constant $[\alpha/\text{Fe}]$) and rightmost (variable $[\alpha/\text{Fe}]$) panels, where the star counts in the lower middle and lower right panels (corrected

⁶We note for completeness that our choice of the range for the variable case ($[\alpha/\text{Fe}] = -0.2$ to $+0.2$) for the four populations was guided by what is known about Carina’s observed values (e.g., Venn et al. 2012 and Paper II).

⁷We note for completeness that we normalized the counts in the background field to those of the program field in several sub-regions in the CMD well away from the Carina principal sequences.

for background) were determined from the synthetic CMDs. These numbers differ slightly from the targets presented in the observed CMD (left panel), due to contamination by other populations. In the lower panels of the synthetic CMDs, the fifth star count corresponds to the box on the upper RGB, and represents the (predicted) cumulative numbers for the four synthetic populations.

Having inspected Figure 7, the reader will immediately realize that we have made no attempt to simulate post-RGB evolution. Insofar as the horizontal branch evolutionary phase is not essential to the problem we are addressing, this is not a serious concern. Of some importance, however, is our neglect of the AGB. As discussed in Section 2.1.1, above $M_V \lesssim -1.0$, the AGB constitutes some 20 – 30 % of stars in the Galactic globular clusters. This is, of course, not the complete story. As the presence of some nine carbon stars in Carina (Azzopardi et al. 1986 and references therein) attests, one should also consider the contribution of AGB stars from intermediate-age populations. To address this issue, we estimated the fraction of AGB on the giant branch using the results of Girardi et al. (2000). For their isochrone having $Z = 0.0004$ ($[\text{Fe}/\text{H}] \sim -1.6$) and age = 7.1 Gyr, we estimate that the AGB represents some 20% of red giant stars in the magnitude range $-2.6 < M_V < -0.7$. We shall return to the question of the absence of AGB from our synthetic CMDs in Section 4, when we compare the number of stars on the upper giant branch of Carina’s observed and synthetic CMDs.

Even so, the astute reader will also note that at best there is only generic agreement between observation and theory in Figure 7: the model produces sharper sequences than are observed; and, indeed, there are three clearly predicted subgiant branches, while only two are observed. We would have to agree. The problem, of course, is that our model of the four putative “basic” populations, each with its unique combination of $[\text{Fe}/\text{H}]$, $[\alpha/\text{Fe}]$, and age, is a gross over-simplification, in the sense that one might expect a spread in age and abundances within each of the basic populations.

3.2.2. *Abundance and Age Spreads within the Four Populations*

The existence of clear sequences (except perhaps for the fourth population) in the observed CMD leads to the expectation that the sizes of the spreads of physical parameters within each of the populations are relatively small. We shall see that moderate age spreads within a given population are more efficient in Carina in producing morphological changes than those in abundance. Previous estimates of age spreads were made in the earliest studies: Smecker-Hane et al. (1996) reported that “bursts” and quiescent phases lasted for $\gtrsim 1$ Gyr, while Hurley-Keller et al. (1998) found that the major intermediate age component

may have lasted as long as 2 Gyr. We now consider the implications of these spreads within the first, second, and third populations.

The First Three Populations

We begin with the tightness of the RGB. As discussed in Section 2.1.1, in the magnitude range $0.0 < M_V < 1.0$ the RGB has an RMS dispersion of $\sigma((B - I)_0) = 0.038$ mag about the quadratic best fit. If we consider the basic Dotter et al. (2008) isochrones adopted for the oldest three synthetic Carina populations in the middle panel of Figure 7 ($[\text{Fe}/\text{H}]/[\alpha/\text{Fe}]/\text{Age} = -1.2/0.1/3.4, -1.5/0.1/7.0, \text{ and } -1.85/0.1/13.2$), for $\sigma((B - I)_0) = 0.038$ mag the corresponding dispersions in $[\text{Fe}/\text{H}]$ in the three populations that could produce the observed dispersion in color are 0.1 – 0.2 dex. If the three populations do not exactly overlap in color in the CMD in the above magnitude range, then in order to reproduce the observed spread in $(B - I)_0$, the inferred individual dispersions in $[\text{Fe}/\text{H}]$ would be even smaller. Variations in age within the three populations should also be considered. Dispersion in age of 1 Gyr at $M_V = 0.5$ on the RGB would lead to dispersions of $\sigma((B - I)_0) \sim 0.03, 0.02, \text{ and } 0.01$ (age increasing), respectively, which would reduce the inferred sufficient dispersion in $[\text{Fe}/\text{H}]$. Variations in $[\alpha/\text{Fe}]$ cause only small changes in $B - I$, and given this relative insensitivity, we choose not to consider the effect of a spread in $[\alpha/\text{Fe}]$ within the diffused populations in what follows. From a different viewpoint, the limits that the tightness of the RGB places on the range in age within the three populations are, roughly speaking, $\sim 1 - 4$ Gyr.

In the absence of obvious strong theoretical constraints on the form of the abundance and age distributions within individual populations and their potential correlations (and for simplicity and convenience) we assumed that each of the oldest three populations has small spreads in $[\text{Fe}/\text{H}]$ and age, which we represent by tophat distributions, about the basic values adopted in Section 3.1.

Figure 8 shows the result when small spreads of fullwidth 0.1 dex and 1.2 – 2.8 Gyr are applied to the basic $[\text{Fe}/\text{H}]$ and age values, respectively, of the oldest three populations in Figure 7. The improvement to the simulations is clear. Of particular interest is that the third population SGB, at $M_V = 2.2$, which is clearly present and was commented upon in discussing Figure 7, is no longer obvious when spreads in $[\text{Fe}/\text{H}]$ and ages are taken into account. Figure 9 further examines the role of the spreads of $[\text{Fe}/\text{H}]$ and age (principally the latter) in diffusing each of the sequences within the CMD. In the figure, the left panel refers to the observations, the middle to the simulations in Figure 7 ($[\alpha/\text{Fe}] = 0.1$) smoothed only by observational errors, and the right to those in Figure 8 ($[\alpha/\text{Fe}] = 0.1$) smoothed by both observational errors and the spreads in $[\text{Fe}/\text{H}]$ and age adopted in that figure. Here one sees clearly the smearing out effect on the third population.

Also superimposed on these panels is a grid that facilitates estimation of the absolute magnitude dispersions on the individual SGBs. The upper panels in the figure plot the number of stars in each of the 35 boxes of the grid, as a function of box number (Z), beginning with the fainter stars. The improvement of the simulations of the SGBs when the small dispersions in $[\text{Fe}/\text{H}]$ and age are included is evident. A further check on the dispersing effect of the age spread for the third population is to count the stars within an appropriate section of the grid in Figure 9. We choose to do this for the bottom 12 boxes of the grid (i.e. over the range $1.7 \lesssim M_V \lesssim 2.3$), where we find that the background-subtracted number of stars, 220, in the observed Carina CMD on the left, compares satisfactorily with the number, ~ 185 , found in each of the two synthetic CMDs in the figure.

The Fourth Population

A challenge for the fourth population is that the color range is surprisingly large, say, $\Delta(B - I)_0 \sim 0.25$ at $M_V = 2.0$, not only in comparison with the observational errors, ~ 0.04 dex, but also with the observed dispersion of the RGB of $\sigma(B - I)_0 \sim 0.04$ at that magnitude (see Section 3.1.2). In order to discuss the difficulties, in Figure 7 we represented the fourth population by the basic isochrones $[\text{Fe}/\text{H}]/[\alpha/\text{Fe}]/\text{Age} = -1.20/0.10/1.4$ and $-1.10/-0.2/1.4$ for the constant and variable $[\alpha/\text{Fe}]$ cases, respectively, and then in Figure 8 broadened the population with tophat filters having fullwidths in $[\text{Fe}/\text{H}]$ and age of 0.1 dex and 1.2 Gyr, respectively, similar to our procedure for the first three populations. Here the color dispersion of the fourth population in the synthetic CMD (variable $[\alpha/\text{Fe}]$ case) in the magnitude range $M_V = 2.0 - 2.4$ is $\sigma(B - I)_0 \sim 0.055 \pm 0.005$, still significantly narrower than the Carina observations, for which the corresponding dispersion is $\sigma(B - I)_0 \sim 0.088 \pm 0.008$.

A basic problem of the simulation is that the synthetic main sequence of the fourth population does not reach as blue as the observations. One limitation of the model might be that it uses isochrones reaching down to only an age of 0.8 Gyr, which is at the low limit of the age range of the stellar isochrones adopted in this work – that is, we cannot reach ages lower than 0.8 Gyr in our simulations. In Figure 8, with a basic synthetic age of 1.4 Gyr and an age spread of 1.2 Gyr about that value we have reached that limit. Younger isochrones are needed to address this problem. Further, in the variable $[\alpha/\text{Fe}]$ case, in the rightmost panels of Figure 8 we have essentially reached the lower limit of $[\alpha/\text{Fe}] = -0.2$ indicated by the observations (Paper II, Figure 20), and the lower limit available in the Dotter et al. (2008) isochrones. In principle, we could force the simulations of the main sequence bluer by decreasing the metallicity. This, however, seems intuitively inappropriate given the monotonically increasing value of $[\text{Fe}/\text{H}]$ as one progresses from first to third populations; that is, at first thought one might expect a higher value than $[\text{Fe}/\text{H}] = -1.1$ to

–1.2 for the fourth population. We shall revisit this problem in Section 3.2.3.

Are there other possibilities? We noted in Section 2 that we thought it unlikely that the fourth population was actually part of Carina’s horizontal branch. Perhaps the HB provides a partial explanation of the observations and we are observing an admixture of a young main sequence and a very faint blue horizontal branch?

A second, and in our view more likely candidate, is that we are observing a young main sequence that has been broadened by stellar rotation. While there is no counterpart of the young, metal-poor main sequence fourth population in the Milky Way, there is a roughly similar component in the intermediate age populous clusters in the Magellanic Clouds. As first pointed out by Mackey et al. (2008), there is a much larger spread in the color of main-sequence turnoff stars in these clusters than can be explained by the photometric uncertainties, which Bastian & de Mink (2009), and Brandt & Huang (2015) have discussed in terms of structural changes in stars with rotation rates that are 20 – 50 % of the critical rotation rate for breakup. See, for example, Figure 1 of Brandt & Huang (2015).

A third possibility, advocated recently by Santana et al. (2016), is that our fourth population comprises blue stragglers of their intermediate age population (our second and third populations). While we are unable to rule out this possibility, we note that their argument holds only at the “1 standard deviation difference” level (see their Section 5.1, Figure 12)⁸.

Our view is that a resolution of the nature of the fourth population will be solved only when spectra of sufficient resolution become available to distinguish between these putative HB stars, blue stragglers, and rotating and non-rotating, metal-poor, main-sequence stars.

3.2.3. Radial Distributions

Further potential insight into the above discussion is provided by consideration of the radial distributions of the four populations, which we present in Figure 10, where we plot the cumulative distributions of the populations as a function of elliptic radius, r_{ellip} . The first thing to note is that the concentrations of the first three populations increase as one goes from the (oldest) first population to the (more recent) third one. In stark contradistinction, however, the concentration of the (putatively youngest) fourth population is less than that

⁸A further complication with this suggestion, in our opinion, is that Carina’s principal population is considerably younger than those of the calibrating systems adopted by Santana et al. (2016) (Sculptor, Draco, Sextans, and Ursa Minor (see e.g. Weisz et al. 2014 and Lee et al. 2009)), calling into question the reliability of their basic calibration).

of any of the older ones. The simplest explanation of this is that there is little if any direct physical connection between the fourth population and the other three. Given the dependences of $B - I$ on $[\text{Fe}/\text{H}]$, $[\alpha/\text{Fe}]$, and age presented above in Section 3.2.2, we conjecture that the metallicity of the fourth population is significantly lower than our first suggestion of $[\text{Fe}/\text{H}] \sim -1.1$, as postulated there.

In Figure 11, for heuristic purposes, we present synthetic CMDs similar in all respects to those in Figure 8 except that the metallicities of the fourth population are lower by $\Delta[\text{Fe}/\text{H}] = 0.3$ dex than in the former. There are two interesting points of difference. First, the main sequence of the fourth population is bluer by ~ 0.10 in Figure 11 than in Figure 8, improving a little the agreement between observation and model. (We note for completeness that the improvement could probably be increased further if we were to have isochrones that reached to ages lower than 0.8 Gyr.) Second, on the red giant branches in the upper panels of the middle and rightmost columns of Figure 11, one sees a handful of stars from the fourth population bluer by $\Delta B - I \sim 0.4$ mag than the RGB at the same M_V (and also that of their counterparts in Figure 8).

The reader may recall that in Section 2.1.1 we pointed out a handful of Carina radial-velocity members in the catalogs of Koch et al. (2006) and Walker et al. (2009b) that fell significantly blueward of the large majority of Carina’s RGB. It is tempting to further conjecture that these observed objects can be identified with stars in our synthetic fourth population.

We realize that the implications of our conjectures are considerable, involving as it does the implicit suggestion that the fourth population has a very different spatial distribution than the third population in an environment that has remained relatively unenriched. We await further targeted observations to see if these suggestions survive rigorous testing.

To conclude this discussion, we note that Kordopatis et al. (2016) have reported that Carina has three populations of red giants which they designate “metal-poor” ($\langle[\text{M}/\text{H}]\rangle = -2.4$), “intermediate-metallicity” ($\langle[\text{M}/\text{H}]\rangle = -1.84$), and “metal-rich” ($\langle[\text{M}/\text{H}]\rangle = -1.0$). They too have found that their most metal-rich component is less centrally concentrated than the more metal-poor populations. Given the different approaches of the two investigations (and not least the resulting different number of components), however, some caution should be exercised in claiming that both investigations have observed the same phenomenon. That said, we note that the Kordopatis et al. (2016) “metal-rich” component comprises 20% (by number) of the red giants studied, while our fourth population represents 6% of the upper RGB (see Section 4).

Given our uncertainty about the metallicity of the fourth population, in what follows we

shall arbitrarily present results for that component for the more metal-rich cases ($[\text{Fe}/\text{H}] = -1.1$ (constant $[\alpha/\text{Fe}]$) and $[\text{Fe}/\text{H}] = -1.2$ (variable $[\alpha/\text{Fe}]$). Insofar as the fourth component is a significantly minority component, this choice will have only a small effect on the results that will be presented.

3.2.4. Comparison of the Ages of This Work with Those of Earlier Investigations

It is of some interest to compare the results of the present work with those of others in the literature. Table 4 presents ages from investigations that have reported multiple populations in Carina, where the data are given to the precision reported by those authors. Our results are presented in the final row. Column (1) gives the authors, while columns (2) – (5) contain the ages (or mean/median values when appropriate) of the populations, in descending order.

Inspection of the table shows that different authors report different numbers of components. This is perhaps not unexpected, insofar as the data for different investigations are of different quality and analyzed in different ways, as a result of which some investigations do not resolve neighboring components or those that are of only minor significance.

What are the essential/common results that one might take from the table?

The Oldest Population

Inspection of Figure 6 and Table 3 of the present work leads to the conclusion that the mean age of the oldest population in Carina’s CMD is not significantly less than 13 Gyr, considerably more restrictive than the comment by de Boer et al. (2014) that “Different studies agree in general that the intermediate-age episode took place somewhere between 3 and 8 Gyr ago and the older episode > 8 Gyr ago, but the exact age and duration of the episodes still remains uncertain”. Our 13 Gyr is also inconsistent with the 7.5 Gyr of Hernandez et al. (2000). That said, in the light of the six results in Table 4 favoring an age greater than 11 Gyr, it seems reasonable to suggest that the median age of the first population lies in the range 11 – 13 Gyr.

How Many Intermediate-Age (2 – 7 Gyr) Populations Are There?

If one sets aside works that present only a (large) age range for the intermediate age population(s), as opposed to distinct components within the adopted limits, there seems to be a reasonable case for two populations in the range 2 – 7 Gyrs.

The Youngest Population?

Four of the nine investigations in Table 4, and in particular those based on recent very high quality faint CMDs, report a very young main sequence component that they have interpreted in terms of a ~ 1 Gyr metal-poor component. This interpretation has been challenged by Santana et al. (2016), who suggest that this putatively young component comprises the blue stragglers of the intermediate-age (2 – 7 Gyr) populations. While we are not persuaded to this position (see our comments in Section 3.2.2), further work is needed to resolve the issue.

3.2.5. The Masses of the Four Populations

One may use the above formalism to directly estimate the masses of the four populations within the elliptical radius, $r_{\text{ellip}} = 13.1'$, under investigation here. Summation over the synthetic CMD brighter than $M_V = 4.5$ for the constant $[\alpha/\text{Fe}]$ case in Figure 7 yields masses of 2820, 6850, 7150, and 2090 M_{\odot} for the first through fourth populations, respectively. Expressed as fractions of the total mass these correspond to 0.15, 0.36, 0.38, 0.11⁹.

As noted in Section 3.2.1, our synthetic CMDs were determined by adopting a Salpeter mass function, $n(m) = n_0 \times m^{-2.35}$, where the number of stars $n(m)$ formed between masses m and $m+dm$ is $n(m)dm$, and n_0 is a constant. It follows that the number of stars, N , in the mass range m_1 to m_2 is $N = n_0/1.35 \times (m_1^{-1.35} - m_2^{-1.35})$, while the total mass of the population in the same mass range is $M = n_0/0.35 \times (m_1^{-0.35} - m_2^{-0.35})$. For each of the four populations we used the stars in the synthetic CMD between appropriately chosen mass limits pertinent to each of the four boxes we adopted to isolate only stars from a given population in order to determine the value of the constant n_0 , and then used the mass equation to determine the total mass of the population (at formation) between the lower and upper mass limits of Carina, for which we adopt 0.1 and $60M_{\odot}$. The resulting total masses of the four populations at their times of formation are then 2.12×10^5 , 2.48×10^5 , 1.42×10^5 , and 0.24×10^5 M_{\odot} (with mass fractions 0.34, 0.39, 0.23, and 0.04)¹⁰. These mass fractions are also presented in

⁹We realize that the use of Salpeter or similar power-law Initial Mass Functions is at odds with what is generally found in the Galaxy for very-low-mass stars, where the IMF is shallower at the low-mass end (e.g., Kroupa 2001). Wyse et al. (2002) have reported a similar result for the UMi dSph. Hence our total mass estimates may be too high. We adopt the Salpeter formalism for consistency with the isochrones we have adopted, and present the above results principally for heuristic purposes.

¹⁰To the reader who is surprised by the apparent disagreement between the relative masses fractions of the four populations in the CMD compared with those over the whole of the assumed IMF, we note that for a given population the ratio is a strong function of the relevant mass range in the CMD over which the

column (5) of Table 3. The coaddition of these masses is $6.3 \times 10^5 M_\odot$, which provides some insight into the total baryonic mass that initially formed stars. It represents the total initial baryonic mass associated with material currently within the $r_{\text{ellip}} = 13.1'$ at the various epochs of formation. We complete this section by noting that de Boer et al. (2014) report that the “total stellar mass formed over the duration of star formation of Carina ... is $0.43 \pm 0.05 \times 10^6 M_\odot$ within the half-light radius of 250 pc” (corresponding to $9.1'$ at a distance of 106 kpc). One should also bear in mind that our values may be overestimates. In low metallicity objects such as Carina, star formation must have been highly inefficient, so large masses would very likely have been lost from the system.

4. THE POPULATION STRUCTURE OF THE UPPER RED GIANT BRANCH

We now use the results of the synthetic CMD presented in Figure 8 to seek insight into the population structure of Carina’s upper giant branch. The breakdown of the populations is shown in Figure 12 for the variable $[\alpha/\text{Fe}]$ case. On the upper RGB the first – fourth populations comprise 14%, 38%, 42%, and 6% of the sample, respectively.

The total number of synthetic stars in the box on the upper giant branch in Figure 8 (119, variable $[\alpha/\text{Fe}]$ case), is somewhat smaller than that observed (169). We have argued in earlier sections that the synthetic result should be increased by 20 – 30% to allow for AGB stars. We would also note here that in the observed Carina CMD in the magnitude range $-1.0 < M_V < 0.0$, there appear to be commensurate numbers of likely AGB and First-GB stars, for which $N_{\text{AGB}}/(N_{\text{AGB}}+N_{\text{First-GB}}) \sim 0.4$. Be that as it may, for a 25% AGB component, the predicted number would increase to 149, only 10% lower than that observed; and given the numbers, a result significant at only the 1.1σ level. Finally, we comment on the question of completeness of the Carina CMD as one goes to faintest magnitudes. While, to our knowledge, no estimates are available in the literature for the present CMD, potential completeness information is available from the deep (g, g-r) photometry of Santana et al. (2016, their Figure 2), from which we estimate 5 – 15% incompleteness over the magnitude range $M_V = 2.5 - 3.3$ of our third through first populations. If this were relevant to the present investigation, it would lead to a decrease of the same order in the predicted number of stars in our upper giant branch box.

The distribution functions of $[\text{Fe}/\text{H}]$, $[\alpha/\text{Fe}]$, and age for the synthetic CMD are presented as generalized histograms in Figure 13 for the variable $[\alpha/\text{Fe}]$ (upper panels) and

determination is made.

fixed $[\alpha/\text{Fe}]$ (lower panels) cases. The results for the four individual populations are shown in different colors as described in the figure caption, while those of the total population have been overplotted in black; Gaussian kernels of 0.15 dex, 0.10 dex, and 0.5 Gyr have been adopted for $[\text{Fe}/\text{H}]$, $[\alpha/\text{Fe}]$, and age, respectively. (Here the smoothing kernels were chosen somewhat arbitrarily, to clearly show the identity and roles of the populations.) We make two comments on the figure. First, as already noted, the bulk of Carina lies at intermediate age. Following our discussion in Section 2.3 on the analysis by Starkenburg et al. (2010) of the Ca II triplet to produce iron abundances, we specifically note here that we find $\sim 75\%$ of the system is younger than 8 Gyr, casting some uncertainty on the abundances of that analysis, insofar as it assumed ages older than that limit. We also comment that it has been suggested that the treatment of age has little effect on $[\text{Fe}/\text{H}]$ abundances determined using the Ca II triplet, based on the work of Cole et al. (2004) and Battaglia et al. (2008). Our concern is that while empirical calibrations of the Ca II triplet are accurately determined for the bulk of old systems within the Galaxy, it is not clear to us that this is the case for a system as complicated in its population structure as Carina. For example, if one plots the Galactic globular and old open clusters studied by Cole et al. (2004, their Table 1), together with the four populations of Carina in our Table 3, in the (Age, $[\text{Fe}/\text{H}]$) – plane, one sees that the second through fourth Carina populations lie far from the Galactic objects. That is, with ages of $\sim 2 - 7$ Gyr and abundances $[\text{Fe}/\text{H}] \sim -1.5$ to -1.15 , the Carina populations lie below the Galactic clusters by 5 – 10 Gyr, and at abundances lower by 0.8 – 1.0 dex – well away from the fundamental Galactic calibrations.

Second, while the differences between the two $[\alpha/\text{Fe}]$ cases are not large for the $[\text{Fe}/\text{H}]$ and age distributions, those for the $[\alpha/\text{Fe}]$ distributions are significantly different, as might be expected. We shall return to this issue in Paper II (Section 10).

The reader will comment that the age Gaussian kernel of 0.5 Gyr in Figure 13 is far too small given the difficulty in determining ages for stars on the RGB from a color-magnitude diagram. A more realistic estimate might be 4.0 Gyr (see, e.g., Paper II), which we adopt here in both upper and lower panels to determine the age distributions in Figure 14 for the constant and variable $[\alpha/\text{Fe}]$ cases. The lack of sensitivity in both panels is obvious. We shall return to a comparison of this distribution with that of the age estimates based on the analysis of the Carina upper giant branch in Paper II.

5. SUMMARY AND DISCUSSION

- We have used the isochrones of Dotter et al. (2008) to produce synthetic CMDs that provide a basic description of four epochs of star formation in Carina, in terms of the

[Fe/H], $[\alpha/\text{Fe}]$, and ages of the four populations, which have $[\text{Fe}/\text{H}] = -1.85, -1.5, -1.2$, and ~ -1.15 and ages $\sim 13, 7, 3.5$, and ~ 1.5 Gyr, respectively, and two $[\alpha/\text{Fe}]$ cases. In the first, $[\alpha/\text{Fe}] = 0.1$ (constant $[\alpha/\text{Fe}]$), while in the second $[\alpha/\text{Fe}] = 0.2, 0.1, 0.0, -0.2$, respectively (variable $[\alpha/\text{Fe}]$). We refer to these as the first through fourth populations (based on their ages) for which details are presented in Table 3. The parameters for the first three populations are strongly constrained by Carina’s well-defined subgiant and main-sequence features together with its very tight RGB. The nature of the fourth population is not so clear, and future work is needed to determine whether a lower value of age and/or $[\text{Fe}/\text{H}]$, blue stragglers, or stellar rotation may also play a role in its position in the CMD.

- A strong (age, metallicity) – relationship emerges from this analysis, in particular for the first through third populations, which is based only on our fitting of four well-defined features in the CMD – distinct subgiant branches of the first and second populations, the conspicuous upper main-sequence stub of the third population, and the small color dispersion observed on the RGB. We shall return to the (age, metallicity) – relationship in Paper II (Section 9).
- As part of the process, we made first order estimates of the spreads in $[\text{Fe}/\text{H}]$ and age for the four basic populations, which are required to explain the spreads in color and magnitude within the principal sequences of the observed CMD. In the absence of other constraints, we assumed that the spreads in these parameters may be described by a tophat function, in which the basic population is spread evenly over the full width of the postulated tophat in $[\text{Fe}/\text{H}]$ and age.

Given the tightness of the RGB, for the first three populations we adopt a full-width for the $[\text{Fe}/\text{H}]$ spread of 0.1 dex, while for the first through third we find acceptable fits by adopting age spreads of 2.8, 2.4, and 2.0 Gyr, respectively. The SGB of the third population (the presence of which is clearly required by the upper main-sequence stub above the SGB of the second population at $M_V \sim 2.7$) is not obvious, resulting from the diffusing effect of its age spread on the stars in the CMD.

For the fourth population we adopt spreads of 0.1 dex in $[\text{Fe}/\text{H}]$ and 1.2 Gyr in age, which do not well-produce the observations, leading as noted above to a need for alternative phenomena to improve the fit.

- One aspect of our four populations that appears to be at strong odds with the results of high-resolution spectroscopic analysis of Carina red giants is the existence of stars having abundances in the range $-2.9 < [\text{Fe}/\text{H}] \leq -2.5$ (Koch et al. 2008 (2), Venn et al. 2012 (2), Lemasle et al. 2012 (1)) (5 unique stars; some 10% of the sample), which

have metallicities considerably below that of our first (oldest and most metal-poor) population which has $[\text{Fe}/\text{H}] = -1.8$.

In our discussion in Section 2.1.1 of available $[\text{Fe}/\text{H}]$ abundances for Carina red giants, we argued that the Ca II-infrared-triplet based $[\text{Fe}/\text{H}]$ abundances of Koch et al. (2006) and Starkenburg et al. (2010) use calibrations which are not applicable to Carina, and suggested it would be better to derive $[\text{Fe}/\text{H}]$ abundances based on model atmosphere line strength calculations of the triplet, together with consistent model atmosphere parameters (in particular, ages) derived from isochrones. These criticisms notwithstanding, we note for completeness that Starkenburg et al. (2010) report that some 10% of Carina’s RGB stars have $[\text{Fe}/\text{H}] < -2.5$.

We shall return to this discussion in Paper II (Section 10).

- The four populations have different radial distributions. The concentrations of the first three increase as one goes from the (oldest) first population to the (more recent) third one. The concentration of the (youngest) fourth population is, however, less than that of any of the older ones. The simplest explanation is that there is little if any direct physical connection between the fourth population and the other three. We conjecture that the metallicity of the fourth population is significantly lower than our adopted value of $[\text{Fe}/\text{H}] \sim -1.15$.
- The mass fractions of the four populations based on stars currently within an elliptical radius of $13.1'$ and extrapolated to their times of formation by assuming a Salpeter mass function, were (in decreasing age order) 0.34, 0.39, 0.23, and 0.04.
- In Paper II we shall present chemical abundances for a sample of 63 Carina RGB stars based on model atmosphere analysis of high-resolution spectroscopy. Comparison in Section 2.1.1 of the position of these stars in the CMD with those of radial-velocity selected samples of Koch et al. (2006) and Walker et al. (2009b) shows that the spectroscopically selected sample is incomplete at the 5 – 10% level, in the sense that it does not include a complete sample of hotter upper giant branch stars. We noted that these bluer objects are most likely AGB stars. We also conjectured in Section 3.2.3 that they may, in some part, be first-RGB members of our fourth (and youngest) population.
- Based on the parameters of the four populations of our synthetic CMDs, we present predicted distribution functions for $[\text{Fe}/\text{H}]$, $[\alpha/\text{Fe}]$, and age for stars on Carina’s upper RGB which provide insight into the relative contributions of the four populations. We shall return to these in Paper II, where we compare them with the results of our investigation of the chemical abundances of our 63 star sample of Carina’s RGB.

We are very pleased to thank P.B. Stetson for making the photometry of Carina available, and to acknowledge very helpful discussions with G.S. Da Costa and A.D. Mackey. Studies at RSAA, ANU, of the Galaxy’s dwarf satellite systems by J.E.N. and D.Y. are supported by Australian Research Council DP0663562, DP0984924, DP120100475, DP150100862, and FT140100554. K.A.V. acknowledges support from the Canadian NSERC Discovery Grants program. This work was partly supported by the European Union FP7 program through ERC grant number 320360.

REFERENCES

- Amarsi, A. M., Asplund, M., Collet, R., & Leenaarts, J. 2015, MNRAS, 454, L11
- Armandroff, T. E., & Da Costa, G. S. 1991, AJ, 101, 1329
- Azzopardi, M., Lequeux, J., & Westerlund, B. E. 1986, A&A, 161, 232
- Bastian, N., & de Mink, S. E. 2009, MNRAS, 398, L11
- Battaglia, G., Irwin, M., Tolstoy, E., et al. 2008, MNRAS, 383, 183
- Battaglia, G., Irwin, M., Tolstoy, E., de Boer, T., & Mateo, M. 2012, ApJ, 761, L31
- Bellini, A., Piotto, G., Bedin, L. R., et al. 2009, A&A, 493, 959
- Bono, G., Stetson, P. B., Walker, A. R., et al. 2010, PASP, 122, 651
- Brandt, T. D., & Huang, C. X. 2015, ApJ, 807, 25
- Campbell, S. W., D’Orazi, V., Yong, D., et al. 2013, Nature, 498, 198
- Cannon, R. D., Hawarden, T. G., & Tritton, S. B. 1977, MNRAS, 180, 81P
- Cannon, R. D., Niss, B., & Norgaard-Nielsen, H. U. 1981, MNRAS, 196, 1P
- Carretta, E., & Gratton, R. G. 1997, A&AS, 121, 95
- Cole, A. A., Smecker-Hane, T. A., Tolstoy, E., Bosler, T. L., & Gallagher, J. S. 2004, MNRAS, 347, 367
- Coppola, G., Marconi, M., Stetson, P. B., et al. 2015, ApJ, 814, 71
- de Boer, T. J. L., Tolstoy, E., Lemasle, B., et al. 2014, A&A, 572, A10
- de Boer, T. J. L., Tolstoy, E., Saha, A., et al. 2011, A&A, 528, A119

- Dolphin, A. E. 2002, MNRAS, 332, 91
- Dotter, A., Chaboyer, B., Jevremović, D., et al. 2008, ApJS, 178, 89
- Dotter, A., Sarajedini, A., Anderson, J., et al. 2010, ApJ, 708, 698
- Fabrizio, M., Merle, T., Thévenin, F., et al. 2012, PASP, 124, 519
- Fabrizio, M., Nonino, M., Bono, G., et al. 2015, A&A, 580, A18
- Girardi, L., Bressan, A., Bertelli, G., & Chiosi, C. 2000, A&AS, 141, 371
- Grillmair, C. J., Mould, J. R., Holtzman, J. A., et al. 1998, AJ, 115, 144
- Grundahl, F., Catelan, M., Landsman, W. B., Stetson, P. B., & Andersen, M. I. 1999, ApJ, 524, 242
- Harbeck, D., Grebel, E. K., Holtzman, J., et al. 2001, AJ, 122, 3092
- Harris, W. E. 1996, AJ, 112, 1487
- Hernandez, X., Gilmore, G., & Valls-Gabaud, D. 2000, MNRAS, 317, 831
- Hurley-Keller, D., & Mateo, M. 2001, in *Astronomical Society of the Pacific Conference Series*, Vol. 245, *Astrophysical Ages and Times Scales*, ed. T. von Hippel, C. Simpson, & N. Manset, 322
- Hurley-Keller, D., Mateo, M., & Nemeč, J. 1998, AJ, 115, 1840
- Irwin, M., & Hatzidimitriou, D. 1995, MNRAS, 277, 1354
- Johnson, C. I., & Pilachowski, C. A. 2010, ApJ, 722, 1373
- Joo, S.-J., & Lee, Y.-W. 2013, ApJ, 762, 36
- Koch, A., Grebel, E. K., Gilmore, G. F., et al. 2008, AJ, 135, 1580
- Koch, A., Grebel, E. K., Wyse, R. F. G., et al. 2006, AJ, 131, 895
- Kordopatis, G., Amorisco, N. C., Evans, N. W., Gilmore, G., & Koposov, S. E. 2016, MNRAS, 457, 1299
- Kraft, R. P., Sneden, C., Smith, G. H., et al. 1997, AJ, 113, 279
- Kroupa, P. 2001, MNRAS, 322, 231

- Lee, M. G., Yuk, I.-S., Park, H. S., Harris, J., & Zaritsky, D. 2009, *ApJ*, 703, 692
- Lemasle, B., Hill, V., Tolstoy, E., et al. 2012, *A&A*, 538, A100
- Mackey, A. D., Broby Nielsen, P., Ferguson, A. M. N., & Richardson, J. C. 2008, *ApJ*, 681, L17
- Majewski, S. R., Frinchaboy, P. M., Kunkel, W. E., et al. 2005, *AJ*, 130, 2677
- Mateo, M., Olszewski, E. W., Pryor, C., Welch, D. L., & Fischer, P. 1993, *AJ*, 105, 510
- Mighell, K. J. 1997, *AJ*, 114, 1458
- Monelli, M., Milone, A. P., Fabrizio, M., et al. 2014, *ApJ*, 796, 90
- Monelli, M., Pulone, L., Corsi, C. E., et al. 2003, *AJ*, 126, 218
- Mould, J., & Aaronson, M. 1983, *ApJ*, 273, 530
- Mould, J. R., Cannon, R. D., Frogel, J. A., & Aaronson, M. 1982, *ApJ*, 254, 500
- Muñoz, R. R., Majewski, S. R., Zaggia, S., et al. 2006, *ApJ*, 649, 201
- Norris, J. E. 2004, *ApJ*, 612, L25
- Norris, J. E., Gilmore, G., Wyse, R. F. G., et al. 2008, *ApJ*, 689, L113
- Norris, J. E., Yong, D., Venn, K. A., et al. 2017, *ApJS*, submitted (Paper II)
- Okamoto, S., Arimoto, N., Yamada, Y., et al. 2008a, in *Astronomical Society of the Pacific Conference Series*, Vol. 399, *Panoramic Views of Galaxy Formation and Evolution*, ed. T. Kodama, T. Yamada, & K. Aoki, 469
- Okamoto, S., Arimoto, N., Yamada, Y., & Onodera, M. 2008b, *A&A*, 487, 103
- Piotto, G., Villanova, S., Bedin, L. R., et al. 2005, *ApJ*, 621, 777
- Saha, A., Monet, D. G., & Seitzer, P. 1986, *AJ*, 92, 302
- Sandquist, E. L., & Bolte, M. 2004, *ApJ*, 611, 323
- Santana, F. A., Muñoz, R. R., de Boer, T. J. L., et al. 2016, [arXiv:1607.05312](https://arxiv.org/abs/1607.05312)
- Shetrone, M., Venn, K. A., Tolstoy, E., et al. 2003, *AJ*, 125, 684

- Smecker-Hane, T. A., Mandushev, G. I., Hesser, J. E., et al. 1999, in *Astronomical Society of the Pacific Conference Series*, Vol. 192, *Spectrophotometric Dating of Stars and Galaxies*, ed. I. Hubeny, S. Heap, & R. Cornett, 159
- Smecker-Hane, T. A., Stetson, P. B., Hesser, J. E., & Lehnert, M. D. 1994, *AJ*, 108, 507
- Smecker-Hane, T. A., Stetson, P. B., Hesser, J. E., & Vandenberg, D. A. 1996, in *Astronomical Society of the Pacific Conference Series*, Vol. 98, *From Stars to Galaxies: the Impact of Stellar Physics on Galaxy Evolution*, ed. C. Leitherer, U. Fritze-von-Alvensleben, & J. Huchra, 328
- Snedden, C., Pilachowski, C. A., & Kraft, R. P. 2000, *AJ*, 120, 1351
- Starkenburger, E., Hill, V., Tolstoy, E., et al. 2010, *A&A*, 513, A34
- Stetson, P. B., Monelli, M., Fabrizio, M., et al. 2011, *The Messenger*, 144, 32
- Tolstoy, E., Hill, V., & Tosi, M. 2009, *ARA&A*, 47, 371
- Vandenberg, D. A., Stetson, P. B., & Brown, T. M. 2015, *ApJ*, 805, 103
- Venn, K. A., Shetrone, M. D., Irwin, M. J., et al. 2012, *ApJ*, 751, 102
- Villanova, S., Geisler, D., Gratton, R. G., & Cassisi, S. 2014, *ApJ*, 791, 107
- Walker, M. G., Mateo, M., Olszewski, E. W., et al. 2009a, *ApJ*, 704, 1274
- Walker, M. G., Mateo, M., & Olszewski, E. W. 2009b, *AJ*, 137, 3100
- Weisz, D. R., Dolphin, A. E., Skillman, E. D., et al. 2014, *ApJ*, 789, 148
- Wyse, R. F. G., Gilmore, G., Houdashelt, M. L., et al. 2002, *New A*, 7, 395
- Zinn, R., & West, M. J. 1984, *ApJS*, 55, 45

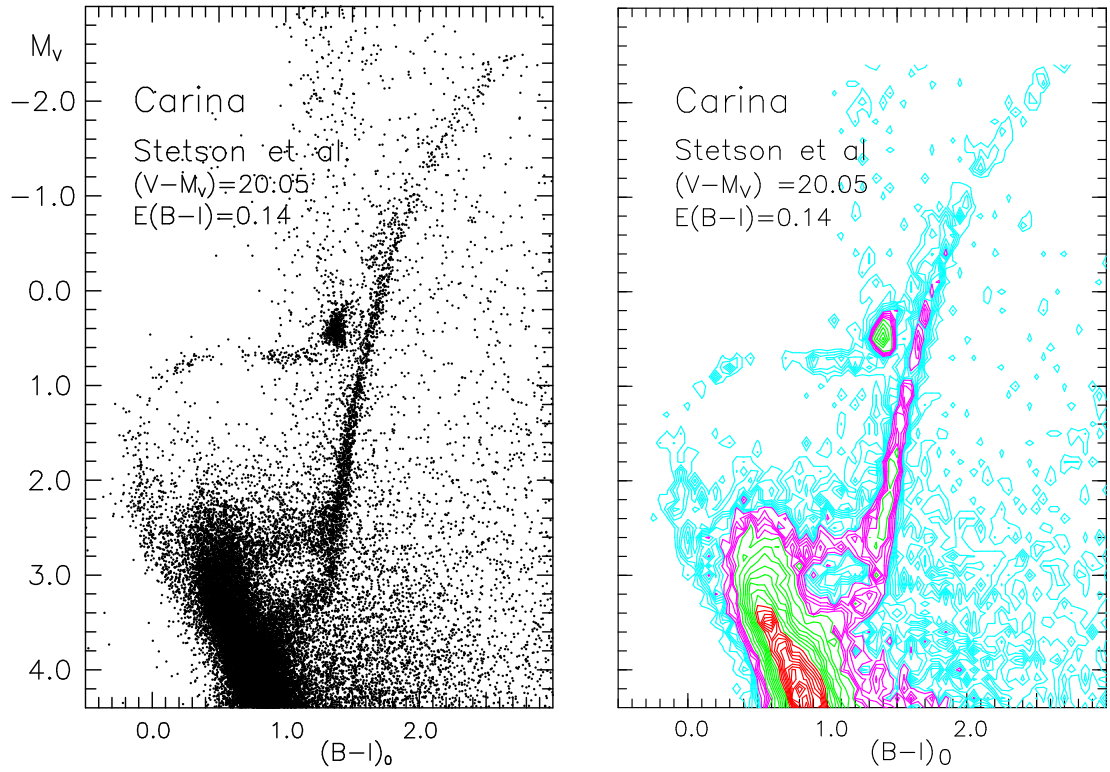


Fig. 1.— The color-magnitude and Hess diagrams of Carina, based on data provided by P.B. Stetson (2014, private communication). The distance modulus and reddening follow Venn et al. (2012).

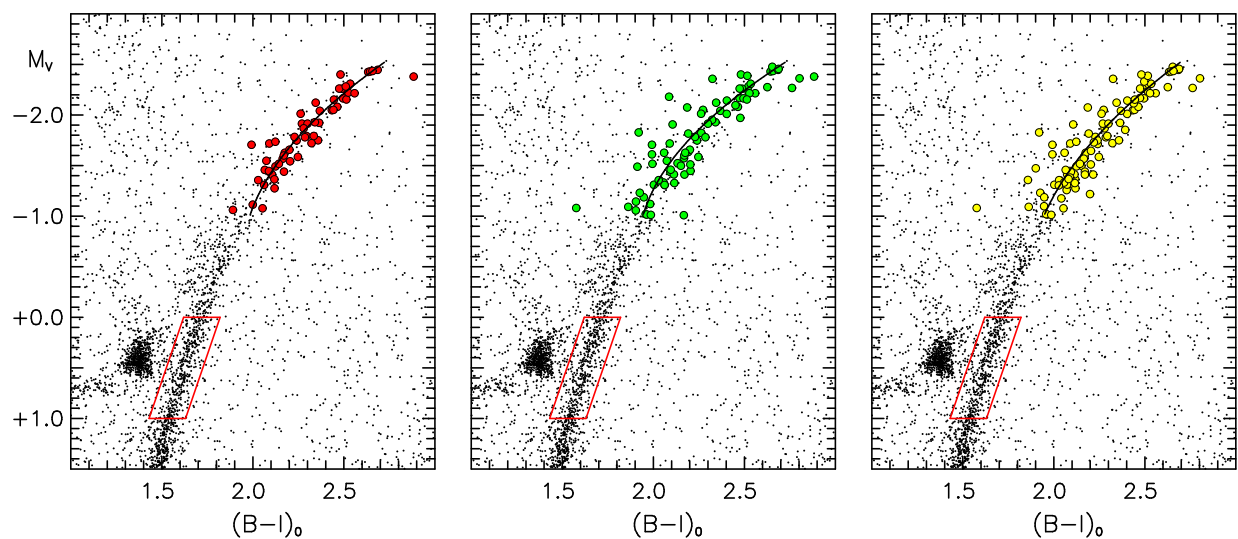


Fig. 2.— The CMD of the upper RGB of Carina, where all symbols present data from Stetson (2014, private communication). On the left the large red circles represent the radial-velocity members of Paper II; in the middle the large green symbols stand for those of Koch et al. (2006); and on the right the large yellow symbols are based on the values of Walker et al. (2009b). The red boxes define a region for which the width of the giant branch has been determined. See text for discussion.

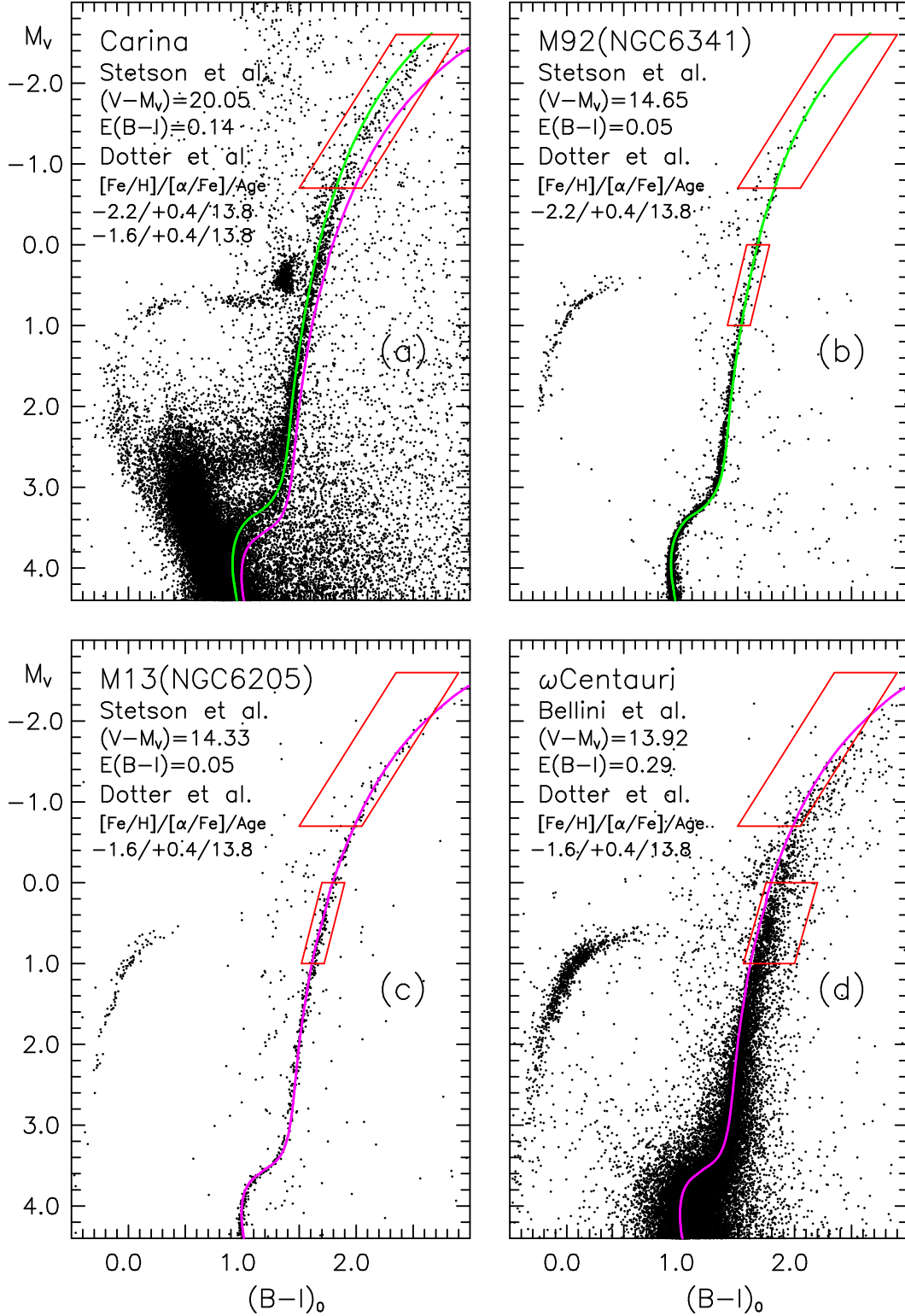


Fig. 3.— Comparison of the color-magnitude diagram of Carina (panel a) with those of M13 (panel c), M92 (panel b), and ω Centauri (panel d). For M13 and M92 the data have been taken from Stetson (<http://www.cadc-ccda.hia-ihp.nrc-cnrc.gc.ca/en/community/STETSON/standards/>), while for ω Cen they come from Bellini et al. (2009). Also overplotted are isochrones from Dotter et al. (2008) for the $[Fe/H]/[\alpha/Fe]/Age$ values included in the legends.

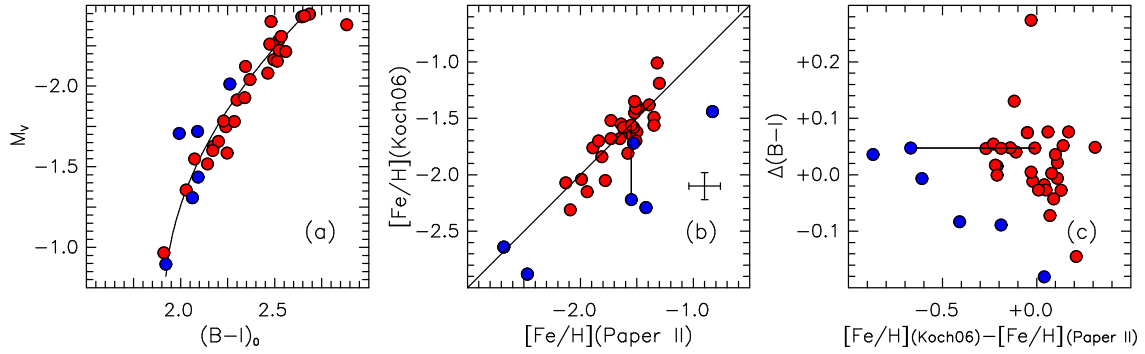


Fig. 4.— Comparison of the $[\text{Fe}/\text{H}]$ values of Koch et al. (2006) (determined by using the infrared Ca II triplet) with the $[\text{Fe}/\text{H}]$ values of Paper II (based on high-resolution spectra). Panel (a) presents the $(M_V, (B-I)_0)$ CMD, together with the quadratic line of best fit; (b) shows $[\text{Fe}/\text{H}]_{\text{Koch06}}$ vs. $[\text{Fe}/\text{H}]_{\text{Paper II}}$; and (c) plots $\Delta(B-I)_0$ (the distance a star falls from the fiducial RGB in the CMD in panel (a)) as a function of the abundance difference $[\text{Fe}/\text{H}]_{\text{Koch06}} - [\text{Fe}/\text{H}]_{\text{Paper II}}$ between the two investigations. The two points joined by the line represent a star presented twice by Koch et al. (2006). See text for a discussion of the blue symbols.

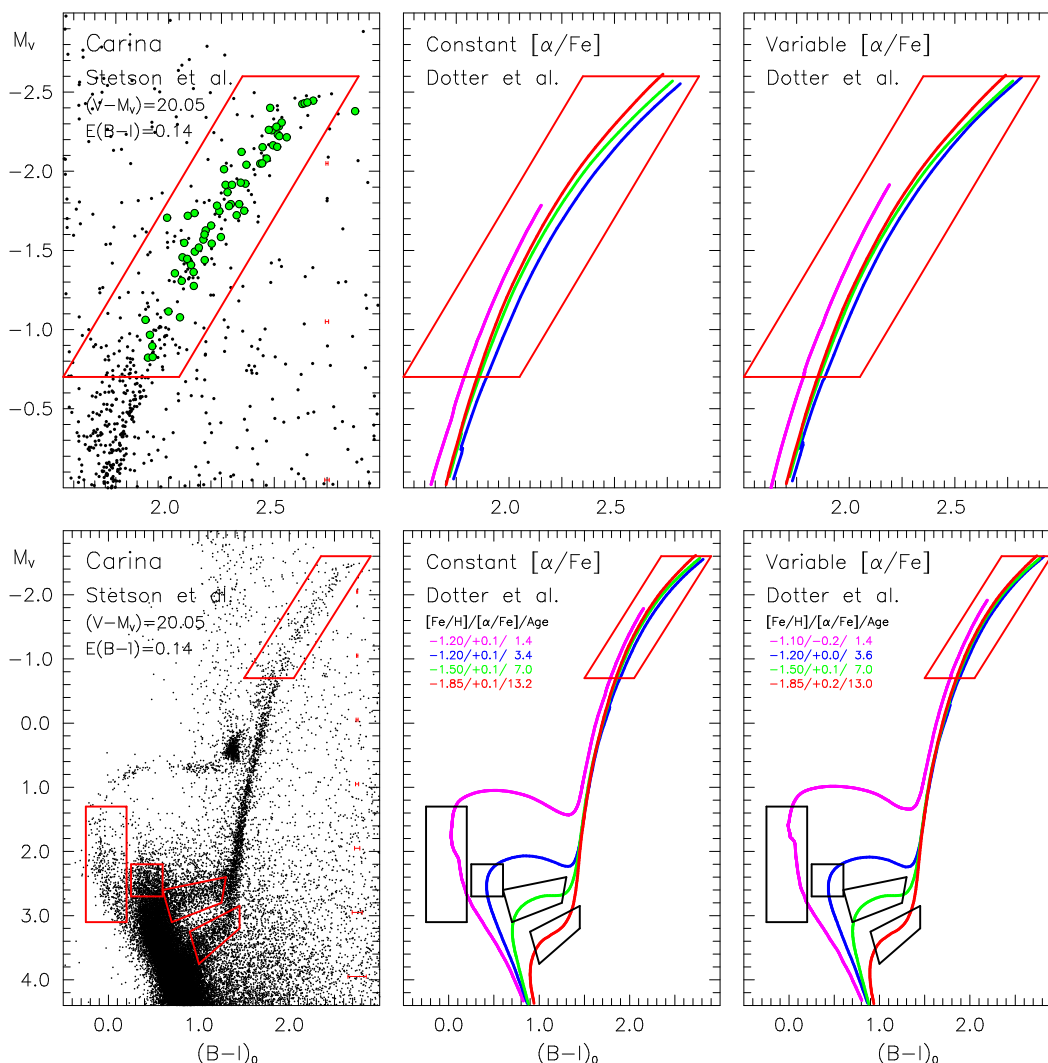


Fig. 5.— Left panels: the observed CMD of Carina as shown in Figure 1, superimposed in the lower panel with four boxes chosen to isolate unique samples of the four basic Carina populations. In increasing brightness from the bottom of the figure these are: (i) the lower subgiant branch (SGB) (at $M_V \sim 3.3$) of the oldest population (the first population); (ii) the upper SGB (at $M_V \sim 2.7$) of the intermediate-age population (second population); (iii) the main sequence stub above the upper SGB (at M_V , $((B-I)_0) = (2.3, 0.5)$), of a younger population (third population); and (iv) the upper, bluer, and somewhat ephemeral main sequence (at $(M_V, (B-I)_0) = (2.0, 0.0) - (3.0, 0.2)$) of the youngest population (fourth population). The fifth and uppermost box in the figure isolates Carina’s upper RGB sample, and (potentially) contains members of all of the above four putative basic populations. In the upper left panel the scale is expanded to permit inspection of the upper RGB in more detail. In both leftmost panels, average magnitude and color error estimates, determined from the values tabulated by Stetson (2014, private communication) are included to the right. Middle and right panels: isochrones from Dotter et al. (2008) that pass in a representative manner through the four population boxes. In the middle panels we hold $[\alpha/\text{Fe}]$ constant, while in the right panels we allow it to vary, decreasing with decreasing age. The population parameters $[\text{Fe}/\text{H}]$, $[\alpha/\text{Fe}]$, and age are shown in the legends.

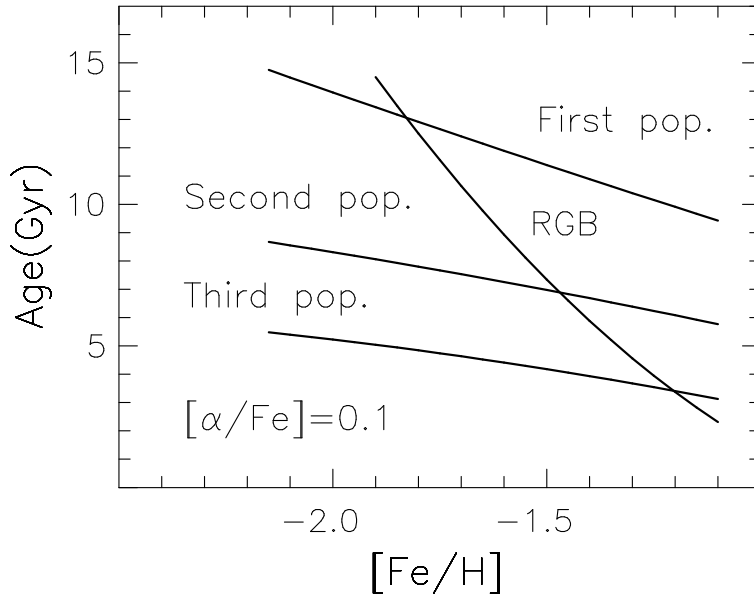


Fig. 6.— Loci of the (age, $[\text{Fe}/\text{H}]$) values for isochrones having $[\alpha/\text{Fe}] = 0.1$ that reproduce the four observable parameters (position of the SGB for the first two populations, the main-sequence stub of the third population, and the collective RGB at $M_V = 0.5$), and are consistent with the positions of the first three populations of the Carina CMD. The loci are generated by the requirement that the basic isochrones pass through $(M_V, (B - I)_0) = (3.25, 1.20)$ (first population), $(2.72, 0.97)$ (second population), $(2.50, 0.42)$ (third population), and $(0.5, 1.62)$ for the RGB. The three intersection points of the four loci define the values pertinent to the first three epochs of Carina. See text for discussion.

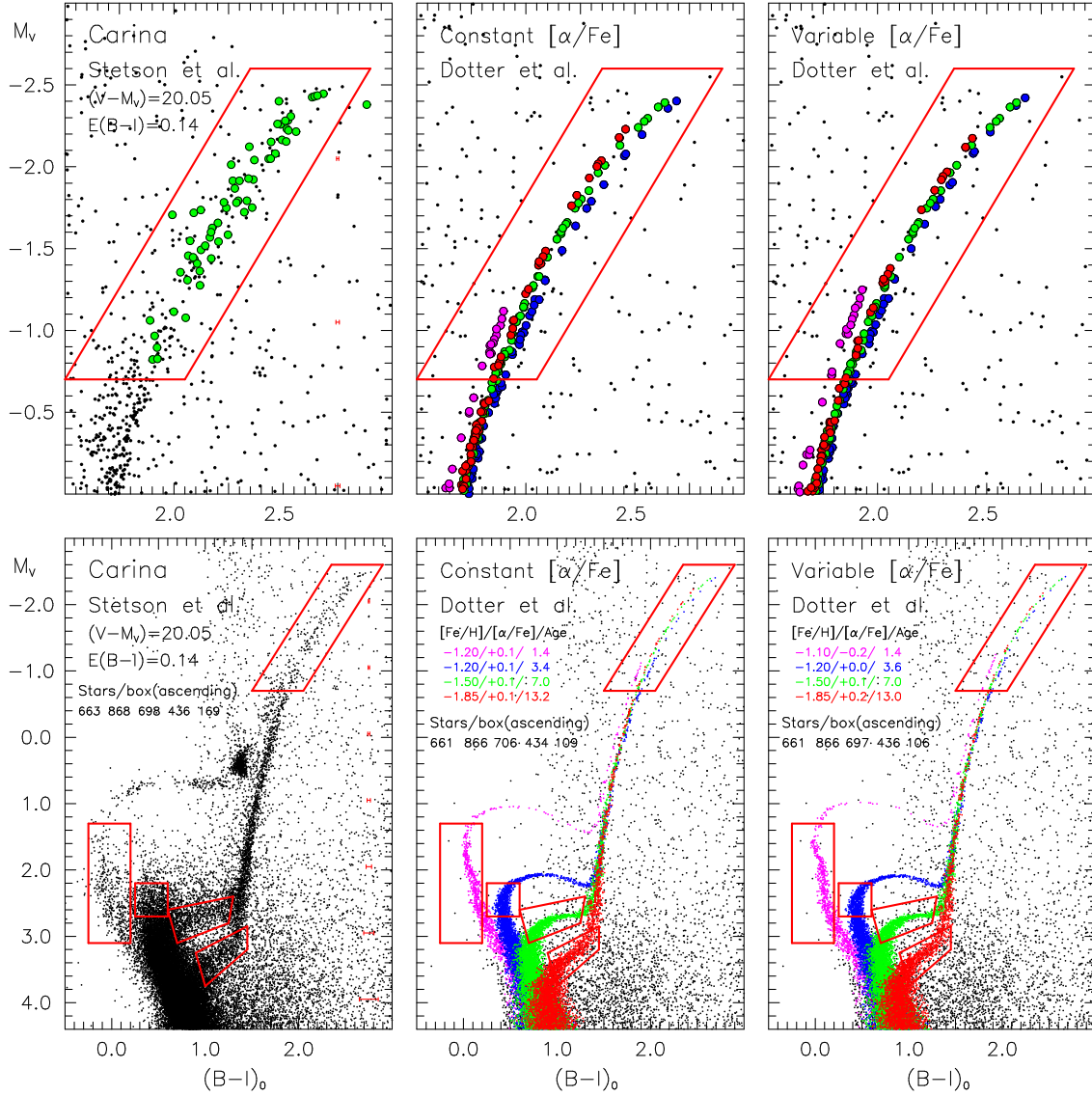


Fig. 7.— The left panels present the observed CMD of Carina as shown in Figure 5, superimposed in the legends of the lower panel with the observed numbers of stars contained in each of the five boxes therein. In the middle and right panels we present synthetic CMDs prepared using the Dotter et al. (2008) isochrones, and adopting magnitude and color errors determined from the Stetson (2014, private communication) tabulated uncertainties, as described in the text. In the middle panels, we hold $[\alpha/Fe]$ constant, while in the right we allow $[\alpha/Fe]$ to vary, as described in the panel legends. In the legend of the lower leftmost panel are the numbers of stars observed in the five sub-samples, corrected for background interlopers by using a nearby field $25'$ from the center of Carina. In the middle and rightmost lower panels the numbers refer to the model results. Note the existence of the subgiant branch at $M_V \sim 2.2$ in the synthetic CMDs, which is not seen in the observations. See text for discussion.

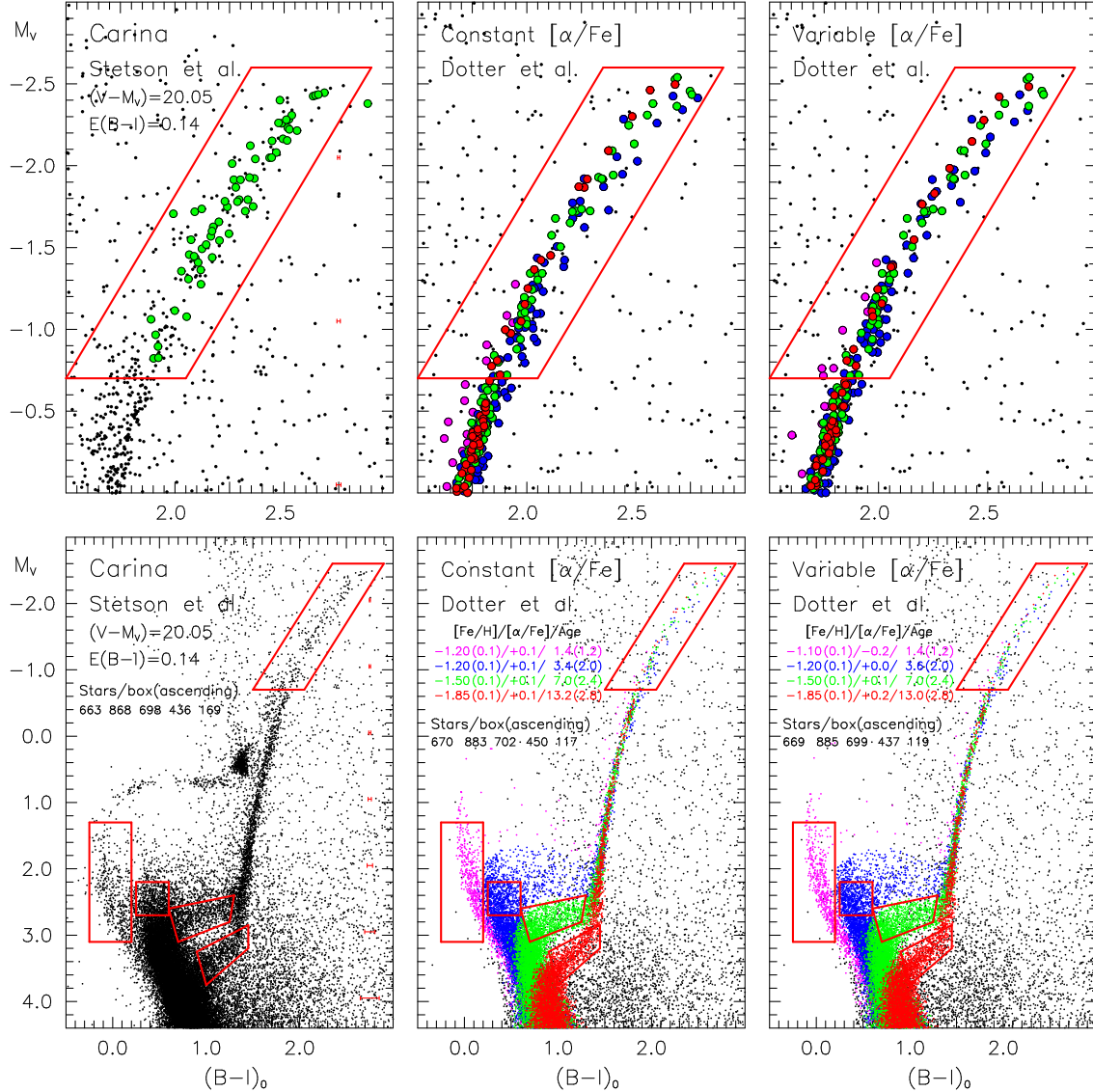


Fig. 8.— Observed and synthetic CMDs, with the same format as used in Figure 7. The synthetic CMDs in the middle and right panels differ from those in Figure 7 in that the synthetic magnitudes and colors have been modified to also randomly simulate the effect of flat ranges in $[\text{Fe}/\text{H}]$ and age about the basic values, by adopting the small ranges shown in parentheses in the legend, as discussed in the text. Note that in the lower panels, these putative spreads in $[\text{Fe}/\text{H}]$ and age have dispersed the subgiant branch at $M_V \sim 2.2$ commented on in the synthetic CMDs presented in Figure 7, to such an extent that it is no longer obvious as a subgiant branch.

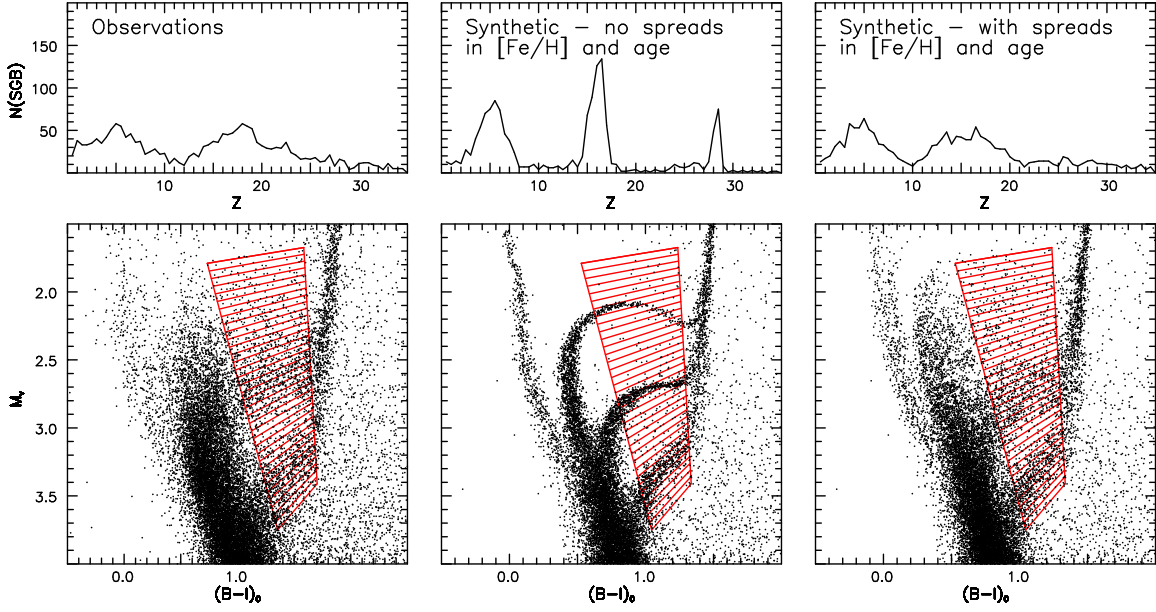


Fig. 9.— Lower panels: comparison between the observed and synthetic CMDs of Carina in the region of the SGBs of the first, second and third populations. The observations are presented on the left, while the synthetic CMDs for the $[\alpha/\text{Fe}] = 0.1$ case from Figures 7 and 8 are shown in the middle (smoothing by only observational errors) and right (smoothing by observational errors and spreads in $[\text{Fe}/\text{H}]$ and age) panels, respectively. Upper panels: $N(\text{SRG})$ vs. Z , where $N(\text{SRG})$ is the number of stars in the individual elongated boxes, and Z represents the box number beginning at the faintest magnitude.

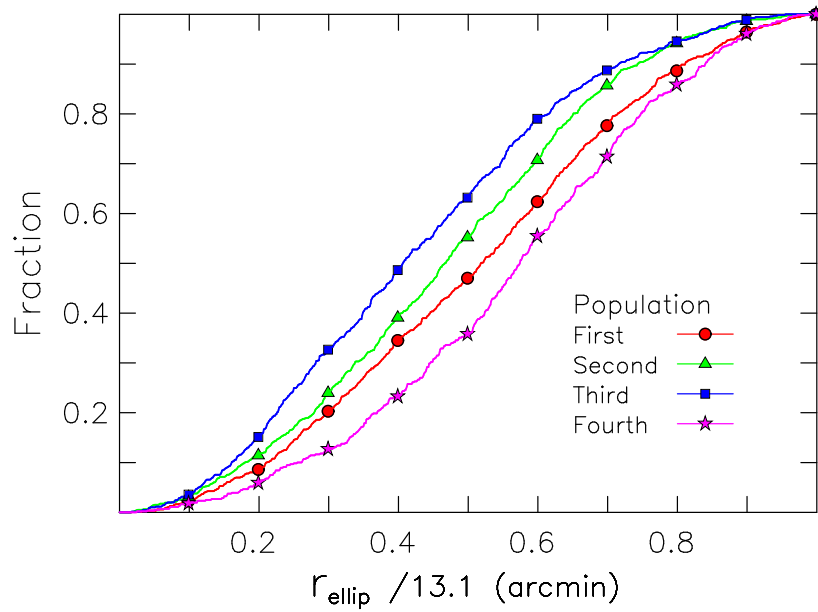


Fig. 10.— The cumulative distribution of the number of stars as a function of elliptic radius r_{ellip} for Carina’s four populations. For the first three populations the concentrations increase as age decreases, while for the (youngest) fourth population, somewhat surprisingly, the concentration is less that for any of the other three. See text for discussion.

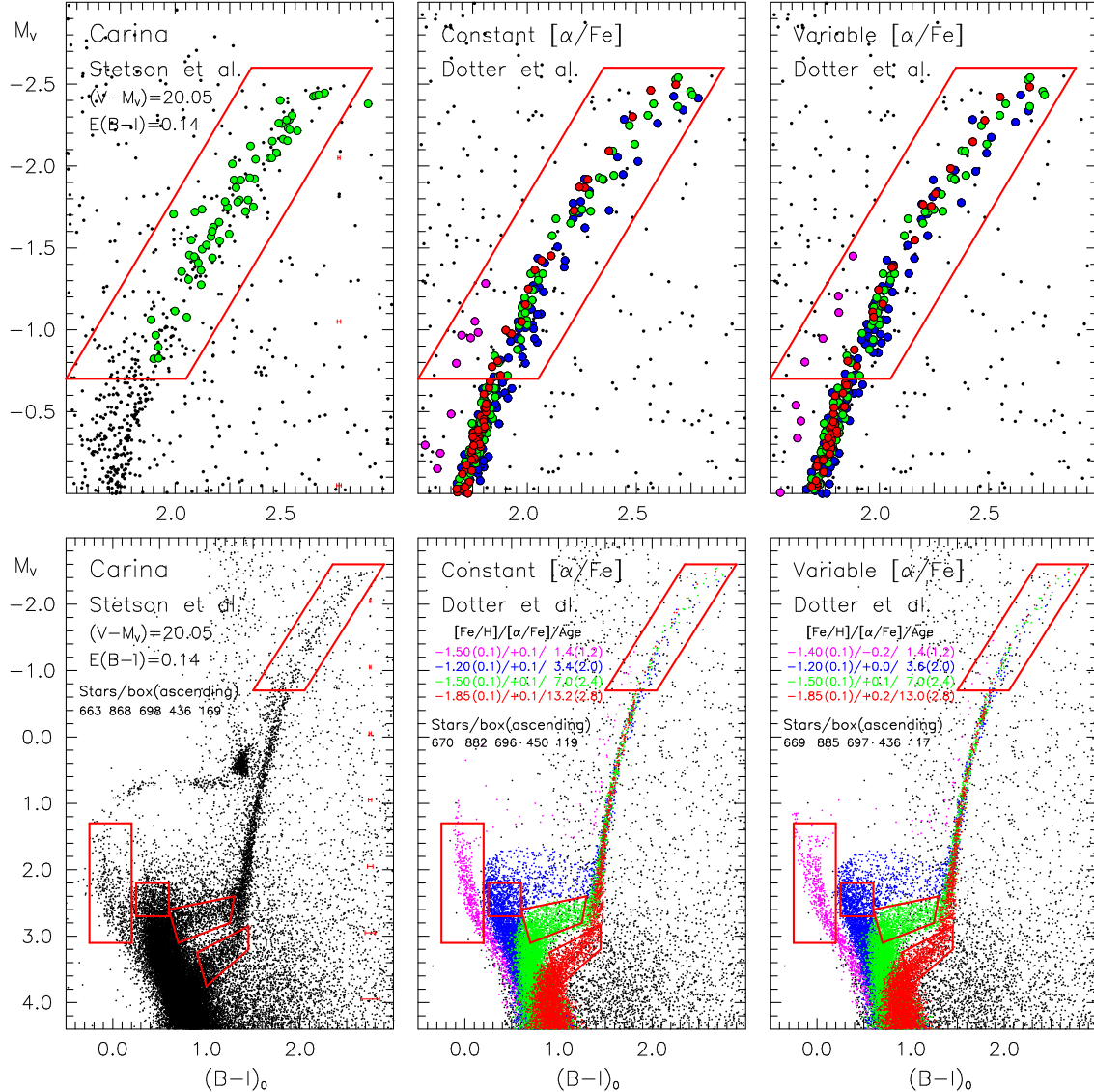


Fig. 11.— Observed and synthetic CMDs, with the same format as used in Figure 8. The parameters of the present figure and Figure 8 differ only in that the basic $[\text{Fe}/\text{H}]$ values for the fourth population have been decreased by 0.3 dex in the former, as shown in the legends. There are two important consequences. First, the main sequence of the fourth population is bluer by ~ 0.10 in the present figure than in Figure 8, and second, in the upper panels of the middle and rightmost columns of the present figure, there is a handful of stars of the fourth population bluer by $(B-I)_0 \sim 0.4$ mag than the bulk of the RGB at the same M_V , considerably larger than that of their counterparts in Figure 8. See text for discussion.

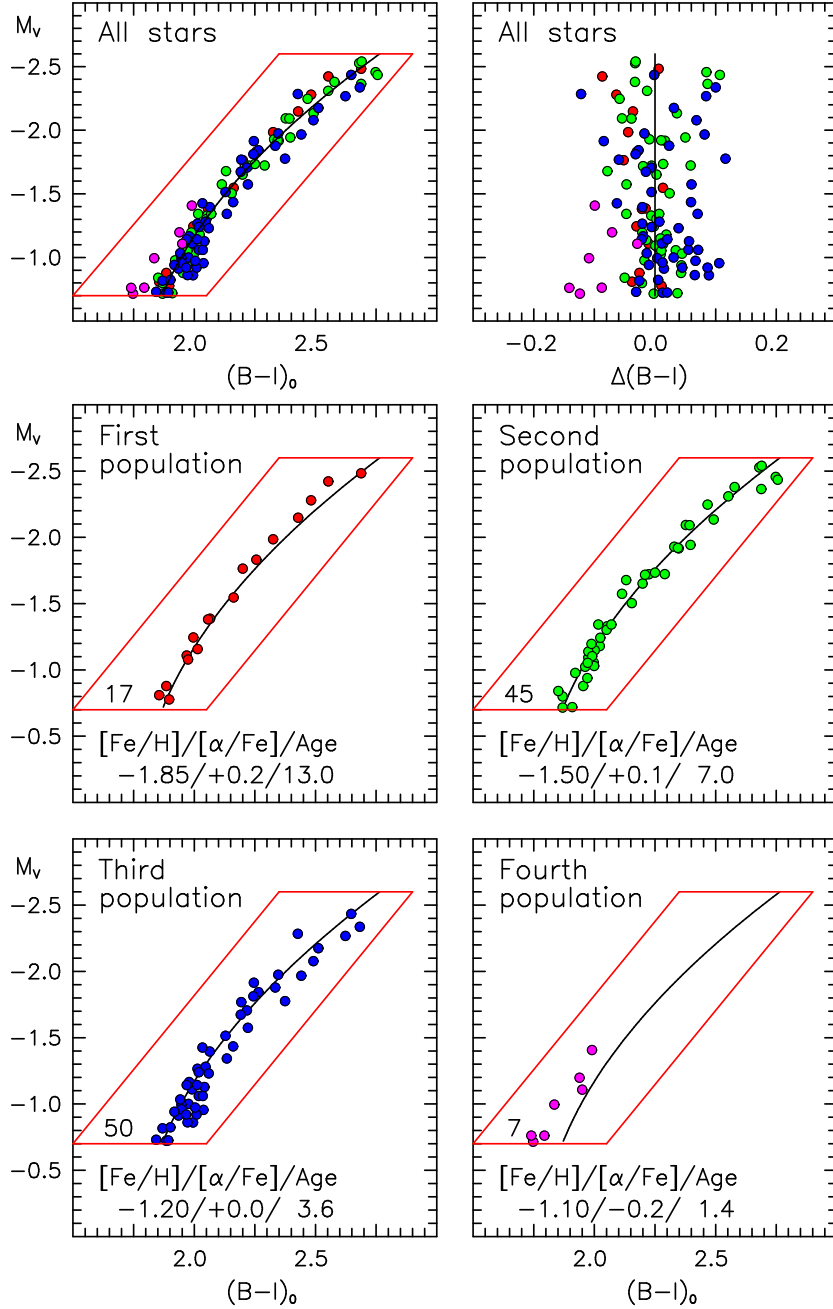


Fig. 12.— The breakdown of the four populations on the Carina synthetic upper RGB (for the variable $[\alpha/\text{Fe}]$ case), where the red box isolates the RGB sample as done in previous figures, and the full lines are the quadratic least-squares best fits to the data. The upper two panels present results for the total sample in the $(M_V, (B-I)_0)$ plane (left) and the $(M_V, \Delta(B-I)_0)$ plane (right), where $\Delta(B-I)_0$ is the distance the star fall away from the line of best fit in the left panel. In the lower four panels, the population parameters and number of synthetic stars are presented for the individual populations (at bottom left of the red box.)

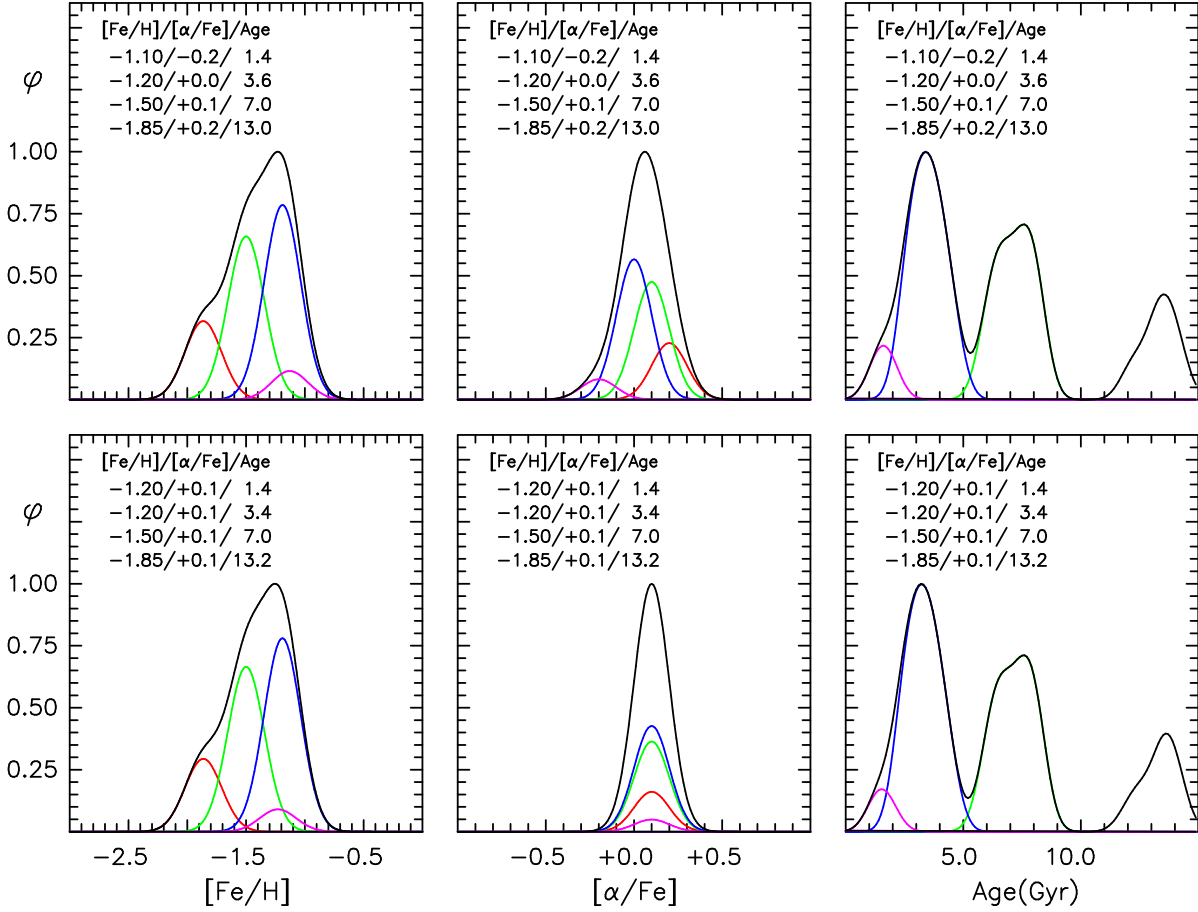


Fig. 13.— Synthetic ($[\text{Fe}/\text{H}]$) MDF, and $[\alpha/\text{Fe}]$ and age distribution functions of the Carina upper RGB, for variable $[\alpha/\text{Fe}]$ (upper panels) and fixed $[\alpha/\text{Fe}]$ (lower panels). Gaussian kernels having σ values of 0.15 dex, 0.10 dex, and 0.5 Gyr, were used for the $[\text{Fe}/\text{H}]$, $[\alpha/\text{Fe}]$, and age distributions, respectively. Red, green, blue, and magenta refer to first through fourth populations, respectively, while their summation is presented in black.

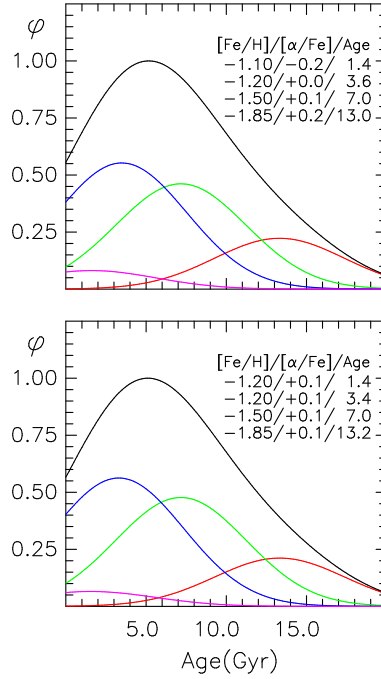


Fig. 14.— Synthetic age distribution functions of the Carina upper giant branch for variable $[\alpha/\text{Fe}]$ (upper panels) and fixed $[\alpha/\text{Fe}]$ (lower panels), where a Gaussian kernel of width $\sigma = 4.0$ Gyr has been adopted, representative of measurement errors on the RGB. As in Figure 13, red, green, blue, and magenta refer to first through fourth populations, respectively, while their summation is presented in black.

Table 1. Major Carina Milestones

Milestone	Authors ^a
The most recently discovered of the Milky Way’s seven classical dSph satellite galaxies	1
Carina possesses some 9 carbon stars	2, 3, 4
First CMD; an intermediate age galaxy	5
RR Lyrae variables, Anomalous Cepheids, and SX Phe stars (currently $\sim 90, 20, 430$)	6, 7
The presence of a significant dark matter component	8, 9
CMD accurate to the main sequence; episodic star formation; three populations	10, 11
Star formation histories (2 – 6 episodes)	12, 13, 14, 15, 16
Radial photometric gradients (driven by age and/or chemical abundance gradients)	14, 17, 18
Large, accurate radial-velocity samples of (hundreds) of RGB members	19, 20
[Fe/H] estimates of large samples of RGB members based on IR Ca II triplet	19, 21
Abundance range based on Ca II triplet: $-3. < [\text{Fe}/\text{H}] < 0.$, $\text{FWHM}_{[\text{Fe}/\text{H}]} = 0.92$	19
High-resolution abundances for RGB samples: $-3. < [\text{Fe}/\text{H}] < 0.$; $0.1 < [\alpha/\text{Fe}] < -0.5$	22, 23, 24, 25, 26, 27
Red giant Car-612 “... formed in a pocket enhanced in SN Ia/II products”	24
Extratidal stars	28, 29, 30
High quality CMDs	31, 32, 33
Very narrow RGB sequence for a system having such large abundance and age ranges	31
Star formation history (two main episodes)	33, 34
The Carina Project	7
Comparison of CMDs with isochrones as a function of age, [Fe/H], and $[\alpha/\text{Fe}]$	35, 36
Chemodynamic sub-populations from medium resolution spectroscopy of ~ 900 stars	37

^aSources: 1 = Cannon et al. (1977); 2 = Cannon et al. (1981); 3 = Mould et al. (1982); 4 = Azzopardi et al. (1986); 5 = Mould & Aaronson (1983); 6 = Saha et al. (1986); 7 = Coppola et al. (2015) and references therein; 8 = Mateo et al. (1993); 9 = Walker et al. (2009a); 10 = Smecker-Hane et al. (1994); 11 = Smecker-Hane et al. (1996); 12 = Mighell (1997); 13 = Hurley-Keller et al. (1998); 14 = Hernandez et al. (2000); 15 = Dolphin (2002); 16 = Monelli et al. (2003); 17 = Hurley-Keller & Mateo (2001); 18 = Harbeck et al. (2001); 19 = Koch et al. (2006); 20 = Walker et al. (2009b); 21 = Smecker-Hane et al. (1999); 22 = Shetrone et al. (2003); 23 = Koch et al. (2008); 24 = Venn et al. (2012); 25 = Lemasle et al. (2012); 26 = Fabrizio et al. (2012); 27 = Fabrizio et al. (2015); 28 = Majewski et al. (2005); 29 = Muñoz et al. (2006); 30 = Battaglia et al. (2012); 31 = Bono et al. (2010); 32 = Stetson et al. (2011); 33 = de Boer et al. (2014); 34 = Santana et al. (2016); 35 = Monelli et al. (2014); 36 = VandenBerg et al. (2015); 37 = Kordopatis et al. (2016)

Table 2. Photometric Internal Errors

V	M_V	$\sigma(V)$	$\sigma(B - I)$
(1)	(2)	(3)	(4)
17.50	-2.55	0.001	0.003
18.50	-1.55	0.002	0.005
19.50	-0.55	0.003	0.008
20.50	0.45	0.004	0.011
21.50	1.45	0.006	0.017
22.00	1.95	0.008	0.024
22.25	2.20	0.009	0.029
22.50	2.45	0.010	0.033
22.75	2.70	0.012	0.040
23.00	2.95	0.016	0.050
23.25	3.20	0.018	0.059
23.50	3.45	0.021	0.068
23.75	3.70	0.026	0.079
24.00	3.95	0.031	0.094
24.25	4.20	0.038	0.111
24.50	4.45	0.042	0.121

Table 3. Basic Isochrones Used to Produce Synthetic CMDs and Deduced Mass Fractions

Population	[Fe/H]	$[\alpha/\text{Fe}]$	Age	Fraction ^a	[Fe/H]	$[\alpha/\text{Fe}]$	Age
(1)	(2)	(3)	(4)	(5)	(6)	(7)	(8)
	Constant $[\alpha/\text{Fe}]$				Variable $[\alpha/\text{Fe}]$		
First	-1.85	0.1	13.2	0.34	-1.85	0.2	13.0
Second	-1.50	0.1	7.0	0.39	-1.50	0.1	7.0
Third	-1.20	0.1	3.4	0.23	-1.20	0.0	3.6
Fourth	-1.20	0.1	1.4	0.04	-1.10	-0.2	1.4

^aPopulation mass fraction (now within 13.1') of Carina at its time of formation

Table 4. Multiple Population Age Estimates (Gyr) from the Literature

(1)	Source	First (2)	Second (3)	Third (4)	Fourth (5)
	Smecker-Hane et al. (1996)	11 – 13	3 – 6	2	...
	Hurley-Keller et al. (1998)	15	7	3	...
	Hernandez et al. (2000)	7.5	4.8	3.3	0.8
	Dolphin (2002) ^a	11.5	6.0	3.0	1.5
	Monelli et al. (2003)	11	5	$\lesssim 1$...
	de Boer et al. (2014)	>8	2 – 8
	Monelli et al. (2014)	12	4 – 8
	Kordopatis et al. (2016)	13	7.5
	Santana et al. (2016)	>10	2 – 8
	This work	13	7	3.5	1.4

^aDolphin (2002) also report a fifth component with age = 0.7 Gyr